GEOLOGICA CARPATHICA, OCTOBER 2022, 73, 5, 411–433 https://doi.org/10.31577/GeolCarp.73.5.2

Pressure–temperature–time constraints on the evolution of epidote-bearing albite granite from Mt. Medvednica (Croatia): Further evidence of the Middle Triassic opening of the Neotethys Ocean

DRAŽEN BALEN[1], PETRA SCHNEIDER[1,✉], JOACHIM OPITZ[2] and HANS-JOACHIM MASSONNE[2,3]

[1]University of Zagreb, Faculty of Science, Department of Geology, Horvatovac 95, 10000 Zagreb, Croatia; drbalen@geol.pmf.unizg.hr, ✉pschneider@geol.pmf.unizg.hr
[2]Universität Stuttgart, Institut für Mineralogie und Kristallchemie (closed), Azenbergstraβe 18, 70174 Stuttgart, Germany; opitz.joachim@web.de, h-j.massonne@imi.uni-stuttgart.de
[3]China University of Geosciences, School of Earth Sciences, State Key Laboratory of Geological Processes and Mineral Resources, 430074 Wuhan, China

(Manuscript received May 23, 2022; accepted in revised form August 31, 2022; Associate Editor: Milan Kohút)

Abstract: Albite granite from Mt. Medvednica in northern Croatia is the only known surface appearance of granite in the complex Zagorje-Mid-Transdanubian zone. This granite contains almost pure albite (An_{01}, ~50–55 vol.%), quartz (~20–25 vol.%), epidote (~1 vol.%), phengite (5–12 vol.%), and secondary chlorite (~10–15 vol.%) and calcite (~5 vol.%). Accessories are zircon, apatite, and ilmenite. The granite has a calc-alkaline geochemical signature with a metaluminous and high-Na character. CaO, MgO, and FeO contents are relatively low. Normalised contents of rare-earth elements (REE) show a relatively flat distribution of those that are heavy, suggesting a magma source in the lower continental crust. The modelled empirical relationship for average crustal thickness based on Sr/Y ratio and contents of REE indicates a 34 km thick continental crust. Zircon typology is characterised by the predominance of {100} prisms and {101} bipyramids. This typology, zircon chemistry, zircon saturation temperature (775 °C), and Ti-in-zircon temperature (mean 785 °C) also suggest a deep-seated magma source. Epidote and perhaps phengite crystallised at a pressure around 1.0 GPa from the melt according to thermodynamic modelling. Temperatures were 650 °C or more at this stage. A U–Pb concordia age of 242.9±4.0 Ma (2σ) was determined on zircon coinciding with the Middle Triassic peak of magmatic activity in the Dinarides, but also in the Southern Alps and Western Carpathians. The age is interpreted as marking the beginning of the fragmentation of continental lithosphere and the onset of rifting processes, which was followed by the broadening of the newly-formed Neotethys Ocean.

Keywords: Triassic, epidote, zircon, granite, Mt. Medvednica, wide-rift evolution

Introduction

Recent research on rocks from Mount (Mt.) Medvednica in Croatia has mainly concentrated on ophiolite-related igneous rocks and the ophiolite mélange with ultramafic rocks, basic intrusives, and volcanic rocks (e.g., Halamić 1998; Babić et al. 2002; Goričan et al. 2005; Lugović et al. 2007; Slovenec et al. 2007, 2010, 2011; Palinkaš et al. 2008; Slovenec & Lugović 2012), as well as low-grade metamorphic rocks (e.g., Judik et al. 2004, 2006; Lugović et al. 2006; van Gelder et al. 2015), that include rare occurrences of high(er)-pressure varieties (Belak & Tibljaš 1998). In addition to the basic objectives, such as determination and definition of rock units and complexes, the focus of this research was on the opening, extension, and closure of the Neotethys oceanic domain. The geological complexity of Mt. Medvednica, combined with the available rock types, dictated the selection of approaches and methods typical for research of ultramafic and mafic igneous rocks, low-grade metamorphic rocks, and fossil-bearing sedimentary rocks. The only known locality where granite occurs (the forested area of Križevna Bukva), has been broadly ignored. Information presented by Majer & Majer (1974), as well as in geological compilations (explanatory notes to the Basic Geological Map: Basch 1981, 1983), including the geological guidebook with maps of Mt. Medvednica (Šikić 1995), provide only basic petrographic information and vaguely-constrained geological ages. Research on the granite by Majer & Majer (1974) revealed the existence of epidote and zircon, which is useful for petrogenetic considerations. These minerals, especially in combination with microtextural characteristics and geochemistry (e.g., Schmidt & Poli 2004 and references therein on epidote; Belousova et al. 2002; Breiter & Škoda 2017 and references therein on zircon), can disclose the (assumed Mesozoic) geological evolution of the addressed area.

The aim of this study is to re-evaluate the petrographic and geochemical characteristics of the albite granite from Mt. Medvednica. Therefore, with this study, we add reliable

constraints to the onset of the Mesozoic geodynamic evolution of a local branch of the Neotethys Ocean. The information on magma evolution and petrogenesis is provided by characteristics of the granite and critical minerals therein. We use new data on epidote chemistry and combine them with the zircon trace and isotopic chemistry to unravel and reconstruct the age, origin, and evolution of the acidic magma as a consequence of the onset of large-scale geodynamic processes.

Geological setting

Mt. Medvednica is positioned in the southwestern part of the Pannonian Basin within the Zagorje-Mid-Transdanubian zone (Pamić & Tomljenović 1998), which forms a large separate unit at the junction of the Alpine and Dinaridic nappe stacks and the Tisia Mega-Unit continental block. This position determines the geological complexity of Mt. Medvednica, which comprises tectonic features of the above-mentioned orogenic chains and block. Various Palaeozoic, Mesozoic and Palaeogene rocks are exposed within the pre-Neogene core, which is a sort of *inselberg* surrounded by Neogene and Quaternary rocks and sediments (Šikić et al. 1978, 1979; Basch 1981, 1983, Fig. 1a–c). The core of Mt. Medvednica comprises four tectonostratigraphic units derived from oceanic and continental realms (Tomljenović 2002): (1) an Eo-Alpine (Cretaceous) metamorphic complex that developed from Palaeozoic–Mesozoic sedimentary and magmatic formations, (2) a Jurassic ophiolitic mélange, (3) a Late Cretaceous–Palaeocene sedimentary sequence (*Gosau cover*), and (4) Triassic clastic and carbonate deposits of the Žumberak–Medvednica Nappe. The regional compressional event, generated by the N-NW-directed ophiolite obduction, caused low-grade metamorphism in Mt. Medvednica during the Early Cretaceous (at 122–110 Ma) as demonstrated by K–Ar ages (Belak et al. 1995).

In the eastern part of Mt. Medvednica, in the area known as Križevna Bukva in the vicinity of the small municipality of Zelina, three small bodies of igneous rocks (in total less than 1 km^2) were mapped and described as albite granite with subordinate varieties of quartz diorite, granophyre, diorite, and keratophyre (Majer & Majer 1974, Fig. 1c inset). These rocks can be found in metamorphosed Lower Permian (?) clastic rocks and Lower Triassic sedimentary rocks (Basch 1981) with a non-discernible contact due to vegetation cover. However, the contact between igneous rocks with the Lower Permian (?) clastic rocks is outlined as tectonic in the geological map, whereas the Lower Triassic clastic and Miocene (Badenian carbonate and clastic) sedimentary rocks are reported to be transgressive over the igneous rocks (e.g., the map in Šikić 1995 as the most recent compilation). In the Geological guidebook of Mt. Medvednica (Šikić 1995), the age of the igneous rocks is marked as Lower Permian–Middle Triassic with a question mark. In fact, Basch (1981) suggested an approximate Lower Permian age; however, it was also noted that the question of age is still open.

The upper Palaeozoic and Lower Triassic sedimentary rocks in the investigated area, as well as in the wider Alpine–Carpathian–Dinaridic context, particularly in the area that became part of the Dinarides, are mainly clastic (e.g., Pamić & Balen 2005, Stampfli & Kozur 2006). At the onset of the Middle Triassic, the geodynamics of the area changed due to the opening of the Neotethys. This led to diversity of depositional environments and intensive magmatic activity forming volcanic and pyroclastic rocks. This Middle Triassic geodynamic activity is related either to continental rifting (e.g., Pamić & Balen 2005) or to convergent movements of lithospheric plates initiated by the subduction of the Palaeotethys (e.g., Stampfli & Kozur 2006).

Analytical methods

Samples and optical investigation

Approximately a dozen samples of acidic igneous rocks from the Križevna Bukva area were collected during field campaigns. Optical investigations were performed on standard thin sections using a Zeiss Axiolab polarising microscope with 25×, 100×, 200×, and 500× magnifications, a Canon EOS 500D camera, and the software packages EOS Utility and AxioVision 4.8.2. Based on the macroscopic field determinations and optical investigations, sample XGO2 (GPS coordinates: N 45.9685°, E 16.1741°) was selected as the representative for thermodynamic modelling, as well as for analyses of the geochemistry of the whole rock and major and accessory minerals. Therefore, the selected sample represents a fixed chemical system for tracing minerals and reactions during its P–T–t evolution.

Whole-rock geochemistry

Sample XGO2 was crushed in a jaw crusher, powdered in an agate mill, and analysed at Bureau Veritas Commodities Canada Ltd (Vancouver) by inductively-coupled plasma mass spectrometry (ICP-MS) for trace elements, while inductively-coupled plasma emission spectrometry (ICP-ES) was used for major elements. Powders were air-dried and sieved through a 0.125 mm stainless-steel screen. The sample preparation included the splitting of 0.2 g rock powder each for $LiBO_2$–$Li_2B_4O_7$ fusion for ICP-ES and ICP-MS. The analytical accuracy was controlled using internal geological reference materials, the compositions of which are comparable to the rocks in this study (STD SO-18/CSC, STD DS7, STD SO-18). Loss on ignition (LOI) was determined by weight difference before and after 4 hours ignition at 1000 °C. The CO_2 content was analysed separately by gravimetry with a Schrötter decomposition apparatus. This content was subtracted from the LOI. The result was attributed to H_2O^+. The obtained geochemical data were processed with the GCDkit software (Janoušek et al. 2006).

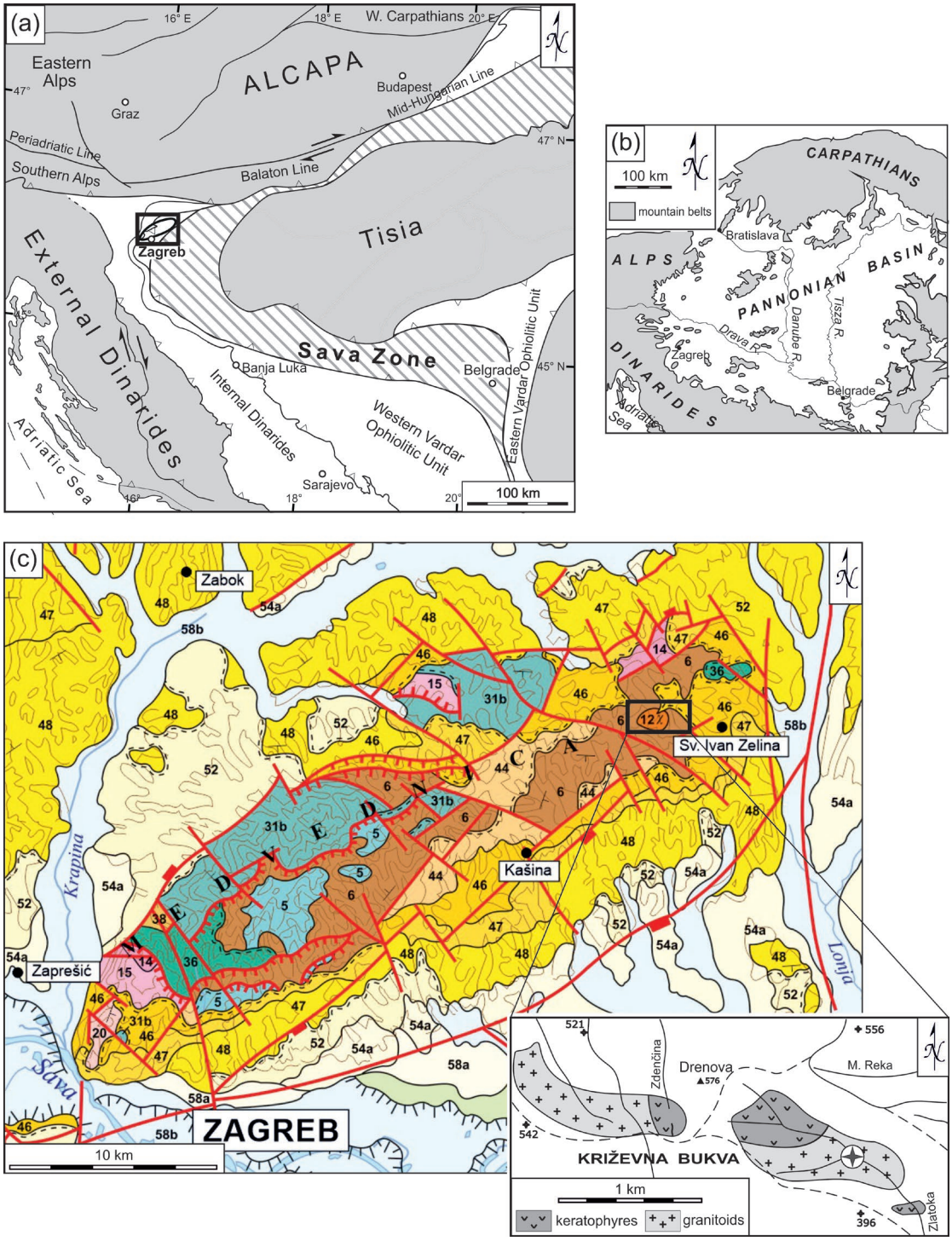

Fig. 1. Simplified maps of (**a**) the Pannonian–Carpathian–Dinaridic–Alpine region showing the major structural units according to Schmid et al. (2008) with the Mt. Medvednica area marked by a quadrangle (the map is slightly modified from Lužar-Oberiter et al. 2012) and (**b**) the mountain belts surrounding the Pannonian Basin. **c** — Geological map of the Mt. Medvednica area (after Croatian Geological Survey 2009) and sketch map of the igneous rocks at Mt. Medvednica (Križevna Bukva locality) from Majer & Majer (1974). The position of the study area is marked by the quadrangle and circled star. Legend: 5 – orthometamorphic rocks (Palaeozoic, ?Triassic); 6 – parametamorphic rocks (Palaeozoic, ?Triassic); 12χ – igneous rocks: quartz-diorites, granodiorites, keratophyres (?Permian); 14 – clastic sedimentary deposits (Early Triassic, *Sajske i Kampilske naslage*); 15 – carbonate deposits (Middle Triassic); 20 – dolomites (Late Triassic: Norian, Rhaetian); 31b – ophiolites: igneous rocks (Middle and Late Jurassic); 36 – carbonate clastic sedimentary deposits (mostly flysch) and *Scaglia* limestones (Late Cretaceous); 38 – carbonate flysch and clastic sedimentary deposits (Palaeocene, Eocene); 44 – clastic sedimentary deposits and carbonates (Miocene, $M_{2,3}$); 46 – *litavac* (bioclastic beech carbonate) and clastic sedimentary deposits with volcanic rocks (Miocene, M_4); 47 – carbonate clastic deposits (Miocene, $M_{5,6}$); 48 – clastic sedimentary rocks and coal (Miocene, M_7); 54a – loess (Pleistocene); 54b – marsh loess (Pleistocene); 57b – marsh deposits (Holocene); 58a – diluvial-proluvial deposits (Holocene); 58b – alluvial deposits (Holocene).

Electron-microprobe analyses of minerals

Chemical analyses and back-scattered electron (BSE) imagery of minerals were performed with the wavelength-dispersive system of a CAMECA SX100 electron microprobe (EMP) at the Institut für Mineralogie und Kristallchemie, Universität Stuttgart, Germany. Operating conditions for quantitative analysis included an accelerating voltage of 15 kV, a beam current of 15 nA, and a beam diameter of about 3 μm. Counting times of 20 s per element at the peak as well as on the background were applied. Natural minerals and pure oxides (albite, periclase, corundum, wollastonite, orthoclase, rutile, rhodonite, fayalite, barite, Fe_2O_3, Cr_2O_3) were used as standards. The PAP correction procedure provided by CAMECA was utilised. A detailed description of the analytical errors is given by Massonne (2012).

Additional analyses of mineral compositions were also obtained with a CAMECA SX100 EMP at the State Geological Institute of Dionýz Štúr in Bratislava, Slovakia. The operating conditions for EMP analysis were 15 kV accelerating voltage, 20 nA beam current, and beam diameters typically between 3 and 5 μm. Standards included minerals, metals, and chemical compounds (wollastonite, TiO_2, Al_2O_3, Cr, fayalite, rhodonite, forsterite, LiF, Ni, V, willemite, NaCl, $SrTiO_3$, barite, orthoclase and albite). Detection limits for major elements are 0.01–0.02 wt.%. The matrix effects were corrected by the conventional ZAF (atomic number-absorption-fluorescence) method.

Scanning electron microscopy

Zircon grains were separated from the sample by a standard procedure of extraction from the host rock: crushing of the rock, sieving, heavy-liquid separation with sodium polytungstate, magnetic separation, and hand-picking. Grains were graphite coated and analysed using the scanning electron microscope (SEM) Tescan Vega TS5136MM, which was equipped with an Oxford Instruments EDS INCA 200 and a BSE detector at the Department of Geology, Faculty of Science, University of Zagreb to detect the external morphology of individual zircon grains. Analyses with the EDS were performed at an accelerating voltage of 20 kV.

Laser ablation–inductively coupled plasma–mass spectrometry (LA-ICP-MS)

Isotopic concentrations of selected elements in zircon were determined by LA-ICP-MS. Analyses were performed at the Institut für Mineralogie und Kristallchemie, Universität Stuttgart (Germany), using an AGILENT 7700 spectrometer after laser ablation with a CETAC LSX-213 laser system. The diameter of the ablated spots was 25 μm. The laser energy was set to 100 % of the maximum (100 %=4 mJ at a spot diameter of 150 μm) at a laser pulse frequency of 10 Hz and 330 (for elemental concentrations) or 375 (for dating) laser pulses per analysis. A mixed He and Ar gas flow with 500 ml/min and 800 ml/min, respectively, served as a carrier of the ablated material into the ICPMS system. Zircon grains separated from the albite granite of Mt. Medvednica had been mounted in an epoxy resin and polished to expose the centre of the grains. Details of the data evaluation methods and corrections are given in Balen et al. (2020).

Chemical analysis of zircon

The standards for the determination of elemental concentrations in zircon were the following glasses: DLH7 and DLH8 from P&H Developments Ltd. and NIST612 and NIST610 from the National Institute of Standards and Technology, USA. The validity of the calibration, data evaluation, and reproducibility were checked with the reference materials Diorite (DRN) and Zinnwaldite (ZW-C) from Service d'Analyses des Roches et des Minéraux du CNRS. Relative elemental concentrations were calculated from the abundance of the corresponding isotope, assuming natural isotopic distributions and individual calibration factors, which were determined under the same experimental conditions. Absolute elemental concentrations were calculated on the basis of the known absolute elemental concentration of an internal reference element.

For the chemical analysis of zircon, the following isotopes were monitored: ^{28,29}Si, ^{31}P, ^{42,44}Ca, ^{49}Ti, ^{51}V, ^{52}Cr, ^{55}Mn, ^{56,57}Fe, ^{59}Co, ^{60}Ni, ^{66}Zn, ^{71}Ga, ^{88}Sr, ^{89}Y, ^{90,91}Zr, ^{93}Nb, ^{118}Sn, ^{137}Ba, ^{139}La, ^{140}Ce, ^{141}Pr, ^{146}Nd, ^{147,149}Sm, ^{151,153}Eu, ^{157}Gd, ^{159}Tb, ^{161,163}Dy, ^{165}Ho, ^{166}Er, ^{169}Tm, ^{172}Yb, ^{175}Lu, ^{177,178}Hf, ^{181}Ta, ^{208}Pb, ^{232}Th, and ^{238}U. All elemental concentrations were calculated relative to Si=15.14 wt.%, a value which is taken as an internal reference value in ideally composed zircon, $ZrSiO_4$, since Si is rarely replaced by other elements in the zircon structure. The concentrations of elements, which are usually not incorporated in zircon, were either very close to the detection limit or clearly elevated and therefore ascribed to inclusions in zircon.

Zircon dating

For zircon dating and isotopic corrections with LA-ICP-MS, the following natural zircon reference materials were used: FC1 (1099.0±0.6 Ma, Paces & Miller 1993), Peixe (564±4 Ma, Dickinson & Gehrels 2003; 558±2.7 Ma, Shaulis et al. 2010), and Plešovice (337.13±0.37 Ma, Sláma et al. 2008). The following masses were measured: ^{202}Hg, ^{204}(Hg+Pb), ^{206}Pb, ^{207}Pb, ^{208}Pb, ^{232}Th, ^{235}U, ^{238}U, and ^{254}UO. Method and corrections used for data evaluation are described in detail in Balen et al. (2020). By dating the reference materials as unknowns using the aforementioned method and corrections, the obtained concordia ages, plotted in the ^{206}Pb/^{238}U vs. ^{207}Pb/^{235}U diagram (FC1=1101.7±14.2 Ma, n=6; Peixe=564.0±7.2 Ma, n=8; Plešovice=338.9±5.0 Ma, n=6; all errors in 2σ), fit well with the literature values.

Geothermobarometry

The classical geothermometric approach applied here includes calculations of the zircon saturation temperature according

to Watson & Harrison (1983), using the whole-rock Zr concentration and the Ti-in-zircon temperatures based on the research by Watson et al. (2006). The latter temperatures were determined from analyses of selected zircon grains that did not show significant Ti-enrichment caused by Ti-rich inclusions.

The PERPLE_X (version 6.8.9, updated February 2020) computer-program package (Connolly 1990, 2005; Connolly & Petrini 2002) was used to calculate pressure–temperature (P–T) fields and vol.% of major minerals and silicate melt in the range of 0.2–1.8 GPa and 600–900 °C for the system Na–Ca–K–Fe–Mg–Al–Si–Ti–H–O. The whole-rock chemical composition of the granite was slightly modified to fit this system as follows: (1) the CaO content was reduced for Ca on the basis of the CO_2 determination and apatite according to the bulk-rock phosphorus content, assuming that this element (P) was bound exclusively to (ideally composed) apatite, (2) 10 % of the Fe was assumed to be trivalent (e.g., Massonne et al. 2007), (3) H_2O was set to 3 wt.%, and (4) the bulk was normalised to 100 wt.%.

The calculations were performed with the thermodynamic dataset hp62ver.dat of Holland & Powell (2011) and the following solid-solution models: cAmph(G) for clinoamphibole (Green et al. 2016), Fsp(C1) for feldspar (Holland & Powell 2003), Ilm(WPH) for ilmenite (White et al. 2000, 2014), Gt(HGP) for garnet and Sp(HGP) for spinel (Holland et al. 2018), Bi(HGP) for biotite, Mica(W) for white mica, Chl(W) for chlorite (White et al. 2014) and Ep(HP11) for clinozoisite–epidote (Holland & Powell 2011). The model melt(HGP) was used for silicate melt (Holland et al. 2018). During calculations, the cAmph(G) solution model reached internal composition limits that were relaxed following software recommendations, whereas Sp(HGP) was rejected from the calculations. Additional calculations with 0.5, 1.0, and 2.0 wt.% H_2O were performed to verify our initial calculation settings including potential shifts of P–T fields for minerals. Further calculations were undertaken to check the influence of a stronger subtraction of CaO from the analysed bulk-rock composition in addition to those mentioned above, because the amount of carbonate in the rock could not be precisely determined.

The P–T diagrams were contoured by isolines of the calculated phase modes using the sub-programs werami and pstable in PERPLE_X. Modal content and composition of phases at specific P–T conditions were calculated with the meemum subprogram. The obtained graphical results were taken as raw data and thus redrawn manually by smoothing curves as demonstrated by Connolly (2005) to produce the final diagrams.

Results

Petrography

The rock is light greyish-green to light green in hand specimens and exhibits a homogeneous granitic texture with medium (0.2–0.5 mm, up to ~1–2 mm) grain size. Textures resulting from intense cataclastic tectonism are also visible.

Microscopic investigation shows that the studied sample is leucocratic, fine- (up to 1mm) to medium- (rarely 1–2 mm in size) grained and isogranular (Fig. 2a,b). The texture of the rock vaguely resembles ophitic varieties of basic rocks. The sample consists of subhedral to anhedral quartz grains (ca. 20–25 vol.%), which are less than 1 mm in size. Equidimensional subhedral to euhedral plagioclase (ca. 50–55 vol.%) occurs with sizes of 0.5–1 mm and rarely above (up to 2 mm). According to the index of refraction, albite to oligoclase forms the partially-altered core regions, whereas the rim is composed of albite. Ferromagnesian minerals, such as chlorite and greenish epidote (Fig. 2c) occur in subordinate quantities. Any evidence of K-feldspar grains is lacking. Granophyric intergrowth between quartz and albite was observed (Fig. 2d). Epidote (ca. 1 vol.%, 100–200 μm in size) forms euhedral to subhedral grains (Fig. 2c–g). White mica (ca. 5–12 vol.%) occurs as single flakes with sizes up to 150 μm (Fig. 2g, Wmc1) as well as in phyllosilicate-rich aggregates inside plagioclase with individual flakes up to 50 μm in size (Fig. 2d,e,g, Wmc2). The larger single flakes are non-oriented and homogeneously-distributed in the rock volume and show sharp contacts with albite and chlorite (Fig. 2g). The phyllosilicate-rich aggregates are accompanied by small (100–200 μm) clinozoisite grains. Epidote and clinozoisite can be distinguished by vivid (epidote) and blue anomalous (clinozoisite) interference colours. All samples taken from the albite granite show these features. Chlorite in randomly-oriented aggregates (ca. 10–15 vol.%, ~200 μm in size, Fig. 2h) is characterised by weak pleochroism of greenish colours. Some of the small, chlorite leaves inside these aggregates show brown, as well as occasional, blue anomalous interference colours. Chlorite aggregates are often accompanied by opaque minerals. Calcite (ca. 5 vol.%) is an interstitial mineral that seems to be of secondary nature. Accessory phases are zircon, apatite, and opaque minerals (ilmenite, Fe-oxide?, pyrite, altogether around 1 vol.%).

Whole-rock geochemistry of the selected sample

The whole-rock analysis of major and trace elements is given in Table 1. The albite granite of Mt. Medvednica shows a moderate SiO_2 (62.5 wt.%) content and high Al_2O_3 (16.7 wt.%) and Na_2O (5.5 wt.%) contents. The dry (without LOI) bulk rock normalised to 100 % classifies the investigated rock as an acidic one with a generally metaluminous character (A/CNK=0.9, A/NK=1.6). The moderate K_2O value (1.1 wt.%) divided by the high Na_2O value results in K_2O/Na_2O=0.2. Further characteristic values are 0.61 for the mafic index MI=$FeO_{tot}/(FeO_{tot}+MgO)$ and 53 for the magnesium number Mg#=mol[$Mg/(Mg+Fe^{2+})$]. The relatively low contents of Fe, given as Fe_2O_3 (3.1 wt.%), MgO (1.8 wt.%), Cr (144 ppm) and Ni (16 ppm) are accompanied by a moderate content of CaO (4.5 wt. %), which is, however, partially due to the presence of (secondary) calcite. Such a chemical composition is typical for calc-alkaline and magnesian rocks. The high LOI

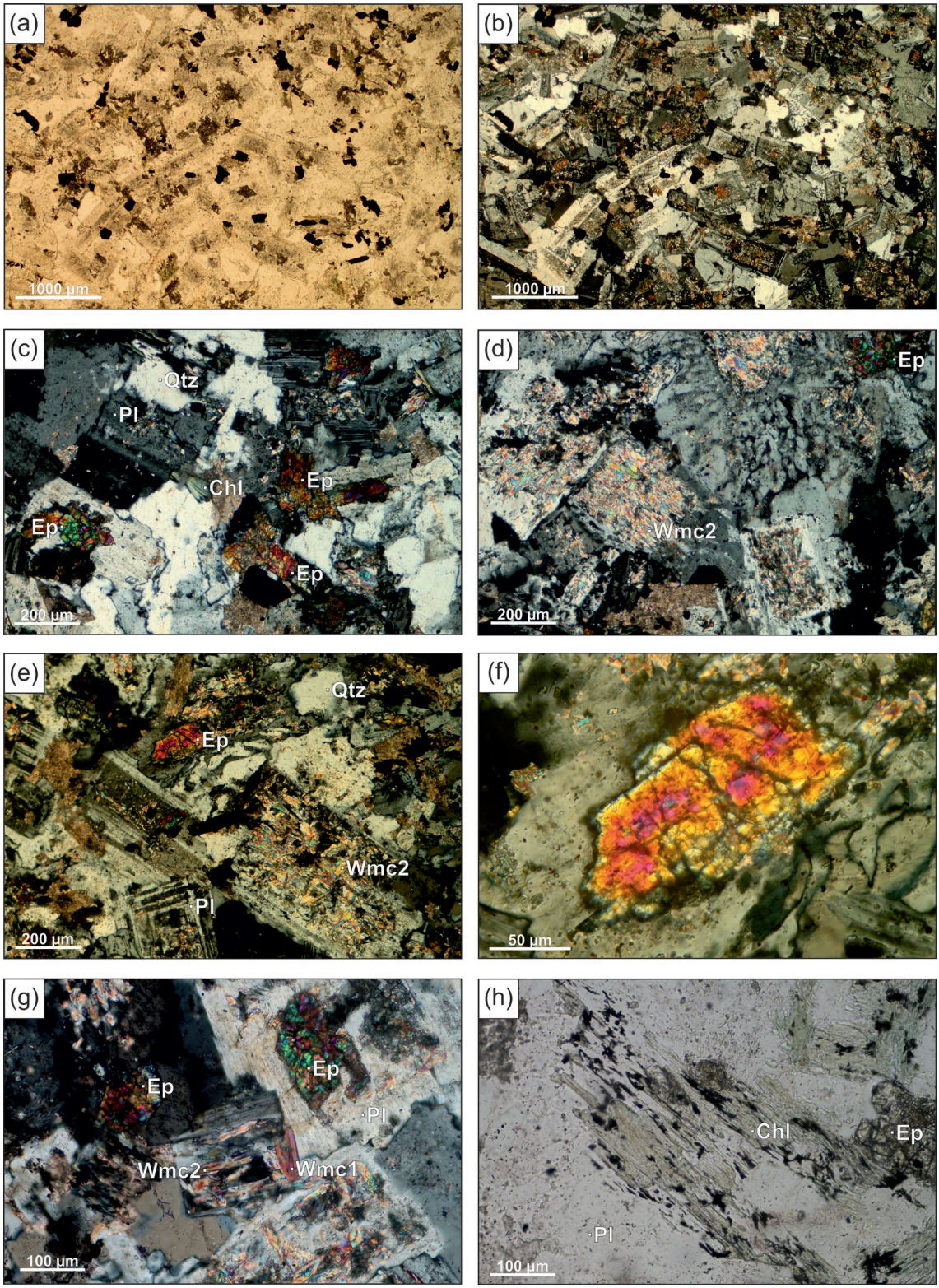

Fig. 2. Photomicrographs under plane-polarised (**a**, **h**) and cross-polarised transmitted light (**b–g**) of typical microfabrics of the Mt. Medvednica granite. **a, b** — Textural relationships of minerals in the studied granite showing predominance of boxy-shaped plagioclase (albite) grains with tiny inclusions of subhedral epidote. **c** — Subhedral to euhedral magmatic epidote in the quartz-feldspar matrix with minor corroded embayments. **d** — Subhedral magmatic epidote (upper right) and secondary minerals (mica and epidote) inside feldspar; magmatic epidote is embedded as single euhedral crystals in the quartz-feldspar matrix, which shows graphic intergrowths. **e, f** — Subhedral to euhedral magmatic epidote showing more intense dissolution by the host granitic magma in contact with feldspar. **g** — Epidote, primary (Wmc1, phengite) and secondary (Wmc2) white mica. **h** — Chlorite aggregate with opaque minerals as a replacement of biotite. Chl – chlorite; Ep – epidote; Pl – plagioclase (albite); Wmc – white mica (Wmc1 – phengite, Wmc2 – secondary mica); Qtz – quartz.

(3.9 wt.%) reflects the CO_2 content in calcite and H_2O contents in white mica, chlorite, and epidote.

The primitive mantle normalisation diagram (Fig. 3a) according to Sun & McDonough (1989) shows an enrichment of incompatible elements 10–60 times higher compared to the primitive mantle, with pronounced positive anomalies of K, Pb, and Zr. The relatively-pronounced negative anomalies of Rb, Nb, P, and Ti are also present. The chondrite-normalised data of rare-earth elements (REE) according to Boynton (1984) (Fig. 3b) reveal a slight enrichment (10–30 times higher compared to the reference chondrite) of light REE relative to heavy REE with characteristic ratios $(La/Yb)_N$=2.6, $(La/Sm)_N$=2.0, and $(Gd/Yb)_N$=1.2. Eu displays a weak negative anomaly (Eu/Eu*=0.83), while no Ce anomaly occurs. The sum of REE is 71 ppm.

Mineral chemistry

The chemical analyses of the minerals are given in Table 2. Epidote, white mica, plagioclase, and chlorite show compositions within a narrow range. The EMP analyses of epidote yield ps=100·Fe^{3+}/(Fe^{3+}+Al) values between 26 and 32 and TiO_2 contents ≤0.05 wt.%, i.e., values characteristic for magmatic epidote (Liou 1973). Epidote cores were identified in polished thin sections using BSE images and EDS spectra to be richer in REE than the rims. Large single flakes of white mica (Wmc1 in Fig. 2) are phengite, characterised by Si=6.66–6.99 atoms per formula unit (apfu) and Mg=0.68–0.80 apfu with X_{Fe}=Fe/(Fe+Mg)=0.18–0.22. Analyses of feldspar outer rims demonstrate that this mineral is almost pure albite (X_{Ab}=0.99) with a slightly more calcic inner region (up to albite-oligoclase). Chlorite has X_{Fe}=0.29. The analysed high Si contents (3.2–3.3 apfu) and the octahedral occupancies that are significantly lower than 6 (5.48–5.61 apfu) point to mixing of chlorite with other phyllosilicates on the submicroscopic scale.

Zircon

Typology

A population of 58 zircon grains was analysed for external morphology. Grains are 60–110 μm long and 25–40 μm wide. The median aspect ratio is 2.6:1. The external zircon

Table 1: Result of the whole-rock analysis: major (wt.%) and trace (ppm) elements with characteristic element ratios and zircon saturation temperature (ZST) from Watson & Harrison (1983). LOI=loss on ignition; MI (mafic index)=FeO_T/(FeO_T+MgO); Mg#=mol [Mg/(Mg+Fe^{2+})]; A/CNK=Al_2O_3/(CaO+Na_2O+K_2O) in mol%; A/NK=Al_2O_3/(Na_2O+K_2O); M (cation ratio)=(Na+K+2Ca)/Al·Si.

Major elements (wt. %)		Trace elements (ppm)		Trace elements – REE (ppm)	
SiO_2	62.48	As	2	La	10.9
Al_2O_3	16.66	Ba	363	Ce	23.4
Fe_2O_3	3.13	Be	2	Pr	3.11
MgO	1.78	Co	5.8	Nd	12.8
CaO	4.46	Cr	144	Sm	3.5
Na_2O	5.49	Cs	1.3	Eu	1.04
K_2O	1.13	Cu	24	Gd	4.17
TiO_2	0.60	Ga	17	Tb	0.69
P_2O5	0.15	Hf	5.5	Dy	4.25
MnO	0.04	Hg	0.07	Ho	0.9
LOI	3.90	Nb	7.2	Er	2.6
SUM	99.84	Ni	19	Tm	0.4
MI	0.61	Pb	3.2	Yb	2.83
Mg#	53	Rb	16.3	Lu	0.38
A/CNK	0.9	Sb	0.1	Sum REE	71
A/NK	1.6	Sc	9	Eu/Eu*	0.83
ASI	0.92	Sn	2	Ce/Ce*	0.97
K_2O/Na_2O	0.2	Sr	226.7	$(La/Yb)_N$	2.6
ZST (°C)	775	Ta	0.6	$(La/Sm)_N$	2.0
M	1.85	Th	4.9	$(Gd/Yb)_N$	1.2
		U	0.9		
CaO (calcite)	3.11	V	57		
CO_2	2.44	W	0.3		
$H2O^+$	1.46	Y	24.5		
		Zn	28		
		Zr	206		
		Zr/Hf	37		
		Sr/Y	9.25		

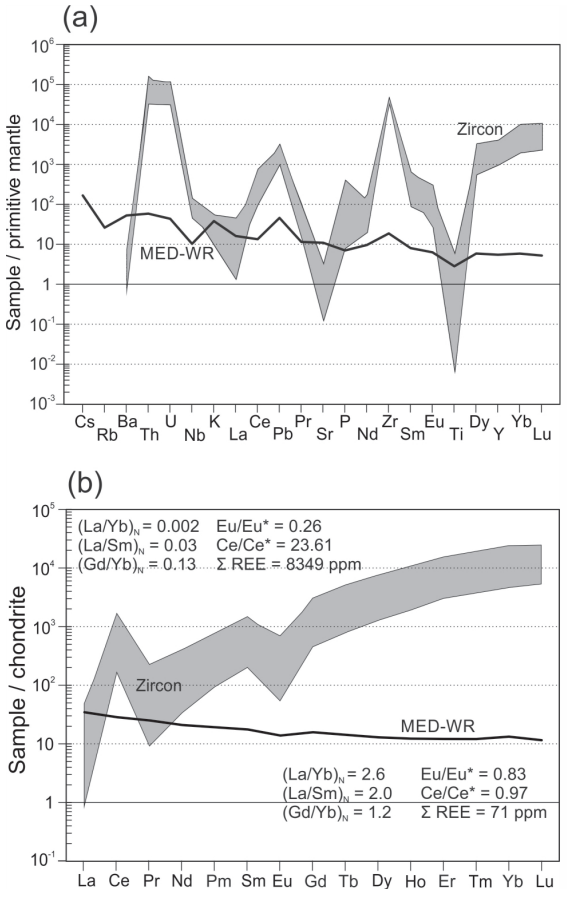

Fig. 3. Primitive mantle-normalised element diagram (**a**) and chondrite-normalised pattern of REE (**b**) for separated zircon grains using normalising factors according to Sun & McDonough (1989) and Boynton (1984), respectively. The part of the whole-rock sample, from which zircon grains were separated, is marked by a bold line.

Table 2: Representative EMP analyses of minerals in the granite from Mt. Medvednica (Križevna Bukva). The structural formulae were calculated on the basis of 12.5 O for epidote, 22 O for white mica (phengite), 8 O for feldspar and 14 O for chlorite. Pistacite content ps=100·Fe^{3+}/(Fe^{3+}+Al), H_2O* – calculated water, X_{Fe}=Fe/(Fe+Mg).

Mineral	Epidote							White mica (phengite)				Plagioclase			Chlorite	
Analysis	1/1	2/1	11/1	#21	#23	#24	#30	#33	8/1	12/1	#22	5/1	15	#27	6/1	10/1
SiO_2	37.61	37.51	37.30	36.93	36.93	37.09	37.22	37.00	50.94	50.49	49.63	68.51	69.49	68.01	34.28	32.80
TiO_2	0.03	0.03	0.05	0.03	0.02	0.00	0.05	0.02	0.05	0.05	0.02		0.00	0.01	0.03	0.06
Al_2O_3	21.41	22.27	21.96	22.95	23.27	21.93	22.10	22.72	27.52	28.25	28.91	19.55	18.87	19.07	21.14	20.57
Fe_2O_3	15.45	14.12	14.64	13.61	12.63	14.71	14.04	13.34	1.63	1.99	1.29	0.10	0.04	0.05	13.01	14.04
MnO	0.06	0.02	0.02	0.37	0.15	0.35	0.10	0.03	0.02	0.04	0.01	0.22	0.09	0.28	0.15	0.13
MgO	0.00	0.00	0.00	0.04	0.01	0.00	0.03	0.02	3.80	4.05	3.39	11.76	11.27	11.91	17.88	18.96
CaO	23.10	23.44	23.22	22.92	23.66	23.16	23.63	23.69	0.05	0.08	0.05	0.05	0.04	0.03	0.58	0.52
Na_2O	0.03	0.02	0.00	0.00	0.01	0.00	0.03	0.03	0.03	0.06	0.08				0.03	0.10
K_2O	0.01	0.00	0.00	0.01	0.01	0.02	0.00	0.01	10.72	10.39	11.36				0.10	0.08
									4.49	4.51	4.47				12.37	12.24
Total	97.70	97.42	97.20	96.87	96.68	97.26	97.19	96.85	99.24	99.90	99.21	100.20	99.79	99.39	99.58	99.48
Si	3.026	3.014	3.009	2.982	2.982	2.997	3.004	2.989	6.810	6.712	6.660	2.990	3.031	2.995	3.324	3.214
Ti	0.002	0.002	0.003	0.002	0.001	0.000	0.003	0.001	1.190	1.288	1.340	0.000	0.000	0.000	0.676	0.786
Al	2.030	2.109	2.088	2.184	2.215	2.088	2.101	2.163				1.005	0.970	0.990		
Fe^{3+}	0.935	0.854	0.889	0.827	0.768	0.895	0.853	0.811	3.146	3.138	3.234	0.004	0.001	0.002	1.741	1.590
Mn^{3+}	0.004	0.001	0.002	0.025	0.010	0.024	0.007	0.002	0.005	0.005	0.002	0.010	0.004	0.013	0.002	0.004
Mg	0.000	0.000	0.000	0.005	0.002	0.000	0.003	0.002	0.182	0.221	0.145	0.994	0.953	1.017	1.055	1.150
Ca	1.991	2.019	2.008	1.983	2.047	2.005	2.043	2.051	0.002	0.005	0.001	0.003	0.002	0.001	0.012	0.011
Na	0.004	0.004	0.000	0.000	0.001	0.000	0.004	0.004	0.756	0.802	0.678	5.007	4.961	5.019	2.585	2.770
K	0.001	0.000	0.000	0.001	0.001	0.002	0.000	0.001	4.091	4.171	4.060				0.060	0.054
H	1.000	1.000	1.000	1.000	1.000	1.000	1.000	1.000							0.006	0.019
O	12.50	12.50	12.50	12.50	12.50	12.50	12.50	12.50	Ca	0.007	0.011	0.008	An	0.01	0.01	0.01	Na	0.006	0.019
									Na	0.008	0.016	0.022	Ab	0.99	0.99	0.99	K	0.013	0.010
ps	31.5	28.8	29.9	27.5	25.7	30.0	28.9	27.3	K	1.829	1.762	1.945	Or	0.00	0.00	0.00			
									X total	1.844	1.789	1.975					sum X	5.475	5.608
																	OH	8.000	8.000
									OH*	4.000	4.000	4.000							
									Total	17.936	17.960	18.035							
									Al total	4.336	4.426	4.574							
									X_{Fe}	0.194	0.216	0.176					X_{Fe}	0.290	0.293

morphology is defined by {100} prisms and {101} bipyramids (Fig. 4). Therefore, according to the zircon typology based on the research by Pupin & Turco (1972) and Pupin (1980), types D and P5 are dominant (for an overview of representative types, see also figure 4 in Balen 2015).

Chemical composition

For zircon geochemistry, 18 grains were successfully analysed with LA-ICP-MS (Table 3). Th/U ratios in zircon range from 0.53 to 4.84 (mean 3.77). Chondrite-normalised patterns of REE in zircon (Fig. 3b) show a significant increase from La to Lu with a mean characteristic ratio $(La/Yb)_N$ of 0.002. A pronounced Ce anomaly $Ce/Ce^*=Ce_N/(La_N \cdot Pr_N)^{0.5}=23.8$ (mean) and a negative Eu anomaly $Eu/Eu^*=Eu_N/(Sm_N \cdot Gd_N)^{0.5}=0.26$ (mean) are discernible. High concentrations of REE (in total 0.28–1.56 wt.%, mean 0.83 wt.%) were also noted.

Dating

Eighteen zircon grains with euhedral shape and without visible inclusions were selected for geochronology. The dating results are presented in Table 4, as well as in a concordia diagram (Fig. 5). The concordia age of 242.9±4.0 Ma (2σ) and a mean square weighted deviation (MSWD) of 2.6 were obtained. Zircon ages resulting from individual calibrated quotients of isotopic intensities (Table 4) are 240.6±4.6 Ma ($^{206}Pb/^{238}U$), 249.8±7.6 Ma ($^{207}Pb/^{235}U$), and 252.6±2.2 Ma ($^{208}Pb/^{232}Th$) with errors given as 2σ values. The three ages coincide within their individual error limits. The MSWD values of 2.4 ($^{206}Pb/^{238}U$) and 9.8 ($^{208}Pb/^{232}Th$) are interpreted to be caused by the presence of slightly different age (sub) groups. However, the MSWD value of 1.3 for $^{207}Pb/^{235}U$ suggests a single zircon generation.

Geothermobarometry and stability of mineral phases

The calculated zircon saturation temperature (Table 1) is 775 °C (with M=(Na+K+2Ca)/(Al·Si)=1.85). Calculations of

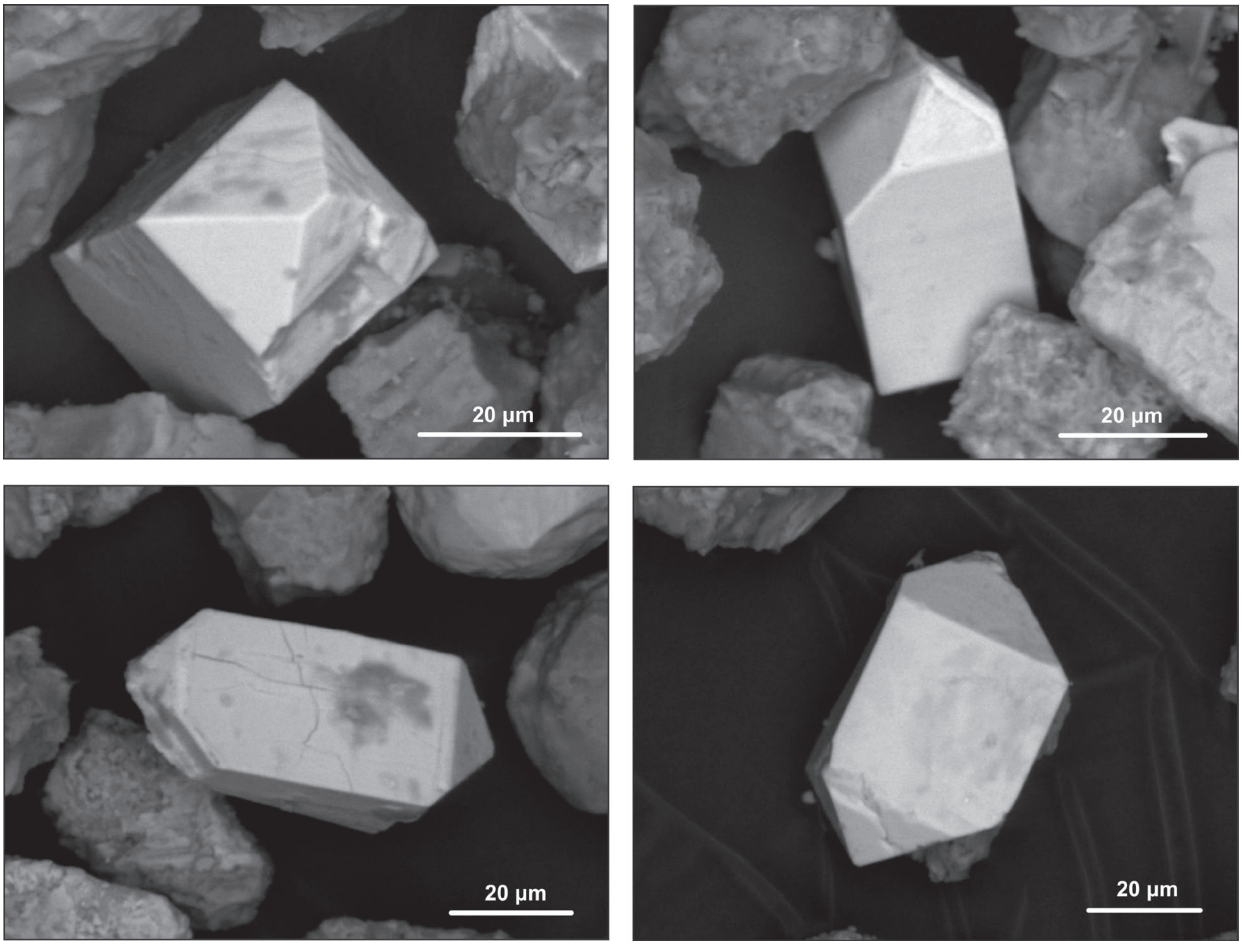

Fig. 4. Typical external morphologies of zircon from the studied granite.

the Ti-in-zircon temperature yielded a range of 726–813 °C (mean 785 °C; Table 3).

The calculated pseudo-section (Fig. 6) and related modes of mineral phases (Fig. 7, Supplementary Fig. S1) for the P–T range 0.2–1.8 GPa and 600–900 °C with 3 wt.% of H_2O shows the following fields for relevant minerals: (1) Plagioclase appears within the whole calculated P–T range except at lower temperatures (600–660 °C) and corresponding pressures above 1.6 GPa (Fig. 7a, b). (2) Although jadeite + quartz is stable on the high-P and low-T range as experimentally demonstrated (e.g., Johannes 1978), pure albite appeared in this range where plagioclase with a higher anorthite content does not occur in the selected P–T range (Fig. 7b). Dashed lines in Fig. 7a, b represent the position of plagioclase (albite) in/out in the CaO non-reduced bulk-rock composition (see chapter Analytical methods: Geothermobarometry), which is shifted toward significantly lower pressures. The modal content of plagioclase increases with decreasing temperature at low pressures. (3) Quartz occupies the whole calculated P–T range with the exception of temperatures higher than 720 °C at low pressures (Fig. 7c). Its modal content increases to a maximum value of 32 vol.% with decreasing temperature and increasing pressure. (4) Epidote (Fig. 7d) appears at P–T conditions above 1.4 GPa and 600–660 °C. However, the P–T field of epidote for the CaO non-reduced bulk-rock composition starts at significant lower pressures – for example, from 0.7 GPa at 600 °C (dashed line in Fig. 7d). (5) The position of the solidus calculated with 3.0 wt.% H_2O starts at ca. 700 °C at 0.2 GPa and reaches 1.8 GPa at ca. 620 °C (Fig. 7e). (6) White mica is stable at temperatures of 600–770 °C and pressures above ca. 0.55 GPa (Fig. 7f).

The calculated mineral phases that are not found in the rock (garnet, amphibole, biotite: Supplementary Fig. S1a–c) represent potential precursors of the late alteration products found in the rock (mainly chlorite). Garnet is stable at P–T conditions above 660 °C and 1.3 GPa and 900 °C and 0.5 GPa. Amphibole is a major hydrous phase and is stable over a wide range of temperatures up to the maximum calculated pressures with the exception of the highest P–T values considered. Its modal content increases with pressure to a maximum of 18 vol.%. Biotite covers the P–T field below 1.6 GPa and 760 °C. The P–T pseudo-section reveals that chlorite is a subsolidus phase, stable at 0.5–0.7 GPa somewhat above 600 °C (Supplementary Fig. S1d). The upper pressure limit of ilmenite is 1.4 GPa at the maximum calculated temperature (Fig. 6).

Table 3: Chemistry of zircon from the studied granite determined by LA-ICP-MS with characteristic element ratios and detection limits (d.l.). Elemental mass concentrations and detection limits are given in ppm. The Si elemental concentration is set as a reference value (151400 ppm). Ti-in-zircon temperature is calculated for the selected grains according to Watson et al. 2006. b.d.l. – below detection limit.

Element	Grain 1a	Grain 2a	Grain 3a	Grain 4a	Grain 5a	Grain 6a	Grain 7a	Grain 8a	Grain 9a	Grain 10a	Grain 11a	Grain 12a
Ba	9.3	11	38	8.6	15	18	30	10	35	b.d.l.	5.7	21
Ca	3257	b.d.l.	9430	10431	5823	1037	3562	1032	2832	b.d.l.	1477	3438
Co	1.3	0.8	1.3	0.8	0.9	1.1	2.4	0.8	2.5	b.d.l.	b.d.l.	2.2
Cr	b.d.l.	b.d.l.	b.d.l.	4.6	4.5	b.d.l.	4.9	4.0	7.3	b.d.l.	b.d.l.	6.3
Fe	5775	3688	5078	2240	4620	3452	9503	3882	7208	178	1223	5300
Ga	1.7	3.5	4.4	3.0	4.0	5.1	5.4	2.2	5.6	b.d.l.	2.1	3.5
Hf	12532	12076	10923	13953	13635	13433	11067	10773	11081	5985	9923	10473
Mn	58	43	142	70	129	136	218	134	186	3.3	26	169
Nb	38	56	63	73	44	79	100	48	101	34	79	75
Ni	b.d.l.	4.2	7.3	b.d.l.	7.6	b.d.l.	b.d.l.	6.9	5.1	b.d.l.	b.d.l.	3.3
P	3010	1802	6020	7904	4839	2372	3368	2011	2833	601	1920	1948
Pb	122	106	103	145	103	161	184	99	184	5.7	153	116
Si	151400	151400	151400	151400	151400	151400	151400	151400	151400	151400	151400	151400
Sn	1.1	2.1	3.9	2.5	2.6	0.8	3.5	1.5	4.3	b.d.l.	1.1	2.3
Sr	7.9	13	19	13	13	13	31	5.7	32	0.9	4.4	17
Ta	22	20	22	36	18	27	34	24	31	6.1	34	28
Th	4821	4872	4648	6628	5459	7315	8505	4264	8989	233	6700	5196
Ti	30	47	98	30	151	45	1551	36	965	18	783	7563
U	1018	1502	1109	1374	1127	1801	2424	1306	2084	440	1671	1384
V	17	16	23	12	21	19	72	11	46	1.6	8.7	22
Y	7125	11513	9762	12423	8303	14376	18356	8841	16487	7930	12258	11872
Zn	95	35	761	66	94	41	105	130	47	b.d.l.	18	49
Zr	487825	496151	389674	510618	502135	504359	494924	433050	493910	502464	496212	484004
La	2.1	14	12	6.7	5.5	6.2	13	3.8	15	0.3	2.6	13
Ce	306	726	702	752	499	828	1338	605	1100	133	772	639
Pr	4.5	14	19	14	14	16	27	8.4	27	1.1	8.6	17
Nd	47	130	153	123	112	159	239	83	237	20	96	118
Sm	64	138	170	145	118	195	284	112	258	50	147	137
Eu	7.3	14	35	22	21	30	41	14	50	15	16	28
Gd	223	455	449	573	285	549	781	348	706	266	567	471
Tb	74	141	126	165	88	171	239	104	204	87	172	138
Dy	769	1416	1158	1557	937	1711	2402	1078	2042	1007	1689	1266
Ho	249	408	323	469	297	522	756	369	602	356	520	360
Er	1099	1710	1273	1790	1337	2166	3178	1605	2494	1386	2178	1561
Tm	227	338	230	321	272	413	604	299	439	264	411	313
Yb	2143	2873	1973	2748	2329	3353	4935	2368	3515	2226	3045	2696
Lu	388	476	338	500	420	587	778	382	617	386	511	501
Sum REE	5602	8853	6961	9186	6736	10708	15614	7377	12305	6197	10134	8257
Sum oxides (wt.%)	104.04	105.13	92.65	110.26	107.13	107.50	108.98	96.04	107.58	102.98	105.30	105.28
HfO_2	14779	14241	12881	16454	16080	15841	13051	12705	13068	7058	11702	12351
Y_2O_3	9049	14621	12397	15776	10545	18257	23311	11227	20937	10071	15567	15076
Th/U	4.73	3.24	4.19	4.82	4.84	4.06	3.51	3.27	4.31	0.53	4.01	3.76
Zr/Hf	39	41	36	37	37	38	45	40	45	84	50	46
Nb/Ta	1.73	2.88	2.83	2.02	2.47	2.90	2.93	1.99	3.23	5.61	2.33	2.62
Ce/Ce*	23.96	12.48	11.19	18.69	13.69	20.01	17.19	25.77	13.16	55.72	39.29	10.35
Eu/Eu*	0.19	0.17	0.38	0.23	0.35	0.28	0.27	0.22	0.36	0.39	0.17	0.34
Hf/Y	1.76	1.05	1.12	1.12	1.64	0.93	0.60	1.22	0.67	0.75	0.81	0.88
La_N/Yb_N	0.001	0.003	0.004	0.002	0.002	0.001	0.002	0.001	0.003	0.000	0.001	0.003
La_N/Sm_N	0.020	0.064	0.045	0.029	0.029	0.020	0.028	0.022	0.036	0.003	0.011	0.059
Gd_N/Yb_N	0.084	0.128	0.184	0.168	0.099	0.132	0.128	0.119	0.162	0.097	0.150	0.141
Yb_N/Sm_N	31	19	11	18	18	16	16	20	13	41	19	18
Ti-in-zircon (°C)										795		

Table 3 (continued)

Grain 13a	Grain 14a	Grain 15a	Grain 16a	Grain 17a	Grain 18a	d.l.	MIN	MAX	Mean	Median	Element
6.5	13	11	9.0	1116	22	0.4	5.7	1116	81	13	Ba
1114	1054	b.d.l.	b.d.l.	1631	1494	767	1032	10431	3401	2231	Ca
0.2	5.5	3.2	0.7	0.7	0.3	0.2	0.2	5.5	1.5	1.0	Co
b.d.l.	8.2	8.2	b.d.l.	b.d.l.	b.d.l.	4	4.0	8.2	6.0	5.6	Cr
257	5112	6080	4823	1347	2760	27	178	9503	4029	4251	Fe
1.4	4.1	5.6	3.0	1.4	b.d.l.	0.7	1.4	5.6	3.5	3.5	Ga
8990	7525	10600	10843	7086	8188	0.05	5985	13953	10505	10808	Hf
6.2	100	201	56	15	30	2	3.3	218	96	85	Mn
48	62	83	68	36	32	0.05	32	101	62	62	Nb
b.d.l.	4.3	6.8	3.3	b.d.l.	b.d.l.	3	3.3	7.6	5.4	5.1	Ni
807	1204	1742	1960	671	753	209	601	7904	2543	1954	P
82	109	160	198	66	70	0.2	5.7	198	120	112	Pb
151400	151400	151400	151400	151400	151400	472	151400	151400	151400	151400	Si
1.4	2.3	2.5	1.6	1.5	1.3	0.7	0.8	4.3	2.1	2.1	Sn
2.6	8.5	9.8	9.6	42	21	0.1	0.9	42	15	13	Sr
19	21	25	28	15	16	0.01	6.1	36	24	23	Ta
3171	5167	6581	8798	2713	2747	0.02	233	8989	5378	5182	Th
8.4	990	50	90	20	21	4	8.4	7563	694	48	Ti
1081	1317	1893	1904	800	647	0.02	440	2424	1382	1346	U
3.4	25	25	34	5.0	6.0	0.4	1.6	72	20	18	V
7591	9718	14922	14306	4852	4367	0.03	4367	18356	10834	10638	Y
6.6	54	229	51	27	8.5	4	6.6	761	107	51	Zn
480932	425110	503851	474588	450189	479441	2	389674	510618	478302	490868	Zr
0.9	6.9	6.0	5.1	1.5	3.5	0.02	0.3	15	6.5	5.7	La
397	656	1143	819	253	173	0.04	133	1338	658	679	Ce
4.0	11	14	13	2.8	4.0	0.03	1.1	27	12	13	Pr
53	90	134	132	26	27	0.08	20	239	110	115	Nd
81	99	169	178	39	39	0.13	39	284	135	138	Sm
4.5	20	14	22	3.9	8.0	0.02	3.9	50	20	18	Eu
327	357	556	632	122	116	0.07	116	781	432	452	Gd
92	108	151	191	45	37	0.01	37	239	130	132	Tb
911	1133	1575	1944	517	405	0.06	405	2402	1306	1212	Dy
297	351	563	603	169	135	0.01	135	756	408	364	Ho
1145	1489	2361	2411	767	625	0.02	625	3178	1699	1583	Er
219	278	449	454	165	122	0.02	122	604	323	306	Tm
1872	2229	3629	3535	1340	953	0.04	953	4935	2653	2532	Yb
330	385	591	596	245	169	0.01	169	778	456	448	Lu
5734	7213	11354	11535	3696	2814		2814	15614	8349	7817	Sum REE
100.96	94.92	107.40	103.47	96.23	100.23		92.65	110.26	103.12	104.59	Sum oxides (wt.%)
10602	8874	12501	12787	8356	9655		7058	16454	12388	12746	HfO2
9640	12341	18950	18168	6162	5546		5546	23311	13758	13509	Y2O3
2.93	3.92	3.48	4.62	3.39	4.25		0.53	4.84	3.77	3.97	Th/U
53	56	48	44	64	59		36	84	48	45	Zr/Hf
2.53	3.00	3.27	2.44	2.35	2.02		1.73	5.61	2.73	2.58	Nb/Ta
50.36	18.12	30.02	24.21	29.71	11.13		10.35	55.72	23.61	19.35	Ce/Ce*
0.09	0.32	0.14	0.20	0.17	0.37		0.09	0.39	0.26	0.25	Eu/Eu*
1.18	0.77	0.71	0.76	1.46	1.87		0.60	1.87	1.07	0.99	Hf/Y
0.000	0.002	0.001	0.001	0.001	0.002		0.000	0.004	0.002	0.001	LaN/YbN
0.007	0.044	0.022	0.018	0.024	0.057		0.003	0.064	0.030	0.026	LaN/SmN
0.141	0.129	0.124	0.144	0.073	0.098		0.073	0.184	0.128	0.129	GdN/YbN
22	21	20	19	32	23		11	41	21	19	YbN/SmN
726				806	813		726	813	785	801	Ti-in-zircon (°C)

Based on the calculated isomodes shown in Fig. 8 and the figures in the Supplementary Fig. S1, the modal proportions of the minerals at P~1.0 GPa and T=650 °C, i.e., P–T conditions at the solidus, are ~50 vol.% plagioclase, ~23 vol.% quartz, ~12 vol.% white mica, ~8 vol.% biotite, ~5 vol.% amphibole, and ~1 vol.% of epidote and opaque minerals each. These values are close to the observed mode when we consider that the chlorite aggregates formed mainly from biotite and secondary calcite at least partially from amphibole at subsolidus conditions.

Table 4: Individual elemental and isotopic concentrations and ages of zircon from the studied granite obtained from the calibrated isotopic ratios of $^{206}Pb/^{238}U$, $^{207}Pb/^{235}U$, and $^{208}Pb/^{232}Th$. The Si elemental concentration is set to the reference value of 15.14 wt.%. The elemental concentration of Pb refers to the sum of all Pb isotopes.

Grain	Elemental concentrations						Isotopic concentrations (ppm)			
	Si (wt. %)	Zr (wt. %)	Th (ppm)	U (ppm)	Pb (ppm)	Th/U	^{204}Pb	^{206}Pb	^{207}Pb	^{208}Pb
1b	15.14000	49.94152	4852.5	1494.3	335.4	3.25	1.82	206.7	14.8	112.1
2b	15.14000	45.26535	4027.6	1604.0	348.9	2.51	6.01	228.1	20.6	94.2
3b	15.14000	50.19822	8103.6	2304.2	500.0	3.52	7.48	303.5	25.2	163.7
4b	15.14000	49.45929	7107.7	1647.6	401.7	4.31	4.91	228.8	19.2	148.9
5b	15.14000	48.55742	6261.4	1434.9	381.3	4.36	2.63	213.9	13.6	151.1
6b	15.14000	50.14567	4100.2	1624.5	344.0	2.52	2.22	232.2	17.3	92.2
7b	15.14000	49.46384	7551.7	2130.3	434.1	3.54	7.59	259.3	20.9	146.3
8b	15.14000	53.91079	6436.9	1306.3	375.1	4.93	3.30	210.1	13.0	148.8
9b	15.14000	52.76371	5971.1	1539.3	408.8	3.88	3.36	239.5	17.0	149.0
10b	15.14000	50.78253	4474.1	1002.6	314.1	4.46	10.30	169.2	20.5	114.0
11b	15.14000	53.00567	3690.5	1158.5	277.0	3.19	6.32	170.6	14.5	85.5
12b	15.14000	51.72661	6065.4	1217.7	371.2	4.98	5.53	198.7	15.2	151.9
13b	15.14000	49.88532	6370.8	1912.2	432.7	3.33	8.09	265.5	20.0	139.1
14b	15.14000	51.58344	4929.4	1146.8	296.0	4.30	2.74	167.7	11.2	114.3
15b	15.14000	48.26227	4679.4	1280.8	307.8	3.65	0.51	191.0	14.8	101.4
16b	15.14000	51.91428	3537.7	825.6	235.7	4.28	2.38	140.9	9.6	82.8
17b	15.14000	51.11619	3501.6	937.8	285.1	3.73	2.63	187.7	11.5	83.2
18b	15.14000	51.59914	6822.9	1852.6	468.2	3.68	5.03	291.9	21.5	149.8

Grain	Isotopic ratios						Age (Ma)					
	$^{206}Pb/^{238}U$	1σ	$^{207}Pb/^{235}U$	1σ	$^{208}Pb/^{232}Th$	1σ	$^{206}Pb/^{238}U$	1σ	$^{207}Pb/^{235}U$	1σ	$^{208}Pb/^{232}Th$	1σ
1b	0.03697	0.00144	0.27136	0.01686	0.01263	0.00027	234.0	8.9	243.8	13.5	254.5	5.5
2b	0.03675	0.00100	0.26915	0.02419	0.01201	0.00037	232.7	6.2	242.0	19.4	241.9	7.5
3b	0.03422	0.00138	0.24533	0.01723	0.01084	0.00037	216.9	8.6	222.8	14.1	218.6	7.5
4b	0.03720	0.00104	0.26345	0.02233	0.01146	0.00019	235.5	6.5	237.4	17.9	230.9	3.8
5b	0.04069	0.00199	0.28355	0.01657	0.01353	0.00039	257.1	12.3	253.5	13.1	272.5	7.7
6b	0.03717	0.00146	0.27027	0.01993	0.01218	0.00015	235.3	9.1	242.9	15.9	245.4	3.0
7b	0.03285	0.00189	0.21720	0.01893	0.01051	0.00038	208.3	11.8	199.6	15.8	211.9	7.6
8b	0.04165	0.00163	0.30416	0.01062	0.01296	0.00024	263.1	10.1	269.6	8.3	261.0	4.8
9b	0.04217	0.00177	0.29206	0.01836	0.01355	0.00020	266.3	10.9	260.2	14.4	272.9	4.0
10b	0.04010	0.00174	0.29389	0.07094	0.01293	0.00040	253.5	10.8	261.6	55.7	260.5	8.1
11b	0.03717	0.00151	0.28083	0.02242	0.01180	0.00060	235.3	9.4	251.3	17.8	237.8	12.0
12b	0.04062	0.00219	0.30942	0.03309	0.01372	0.00024	256.7	13.6	273.7	25.7	276.2	4.7
13b	0.03674	0.00245	0.26643	0.02167	0.01197	0.00027	232.6	15.2	239.8	17.4	241.3	5.5
14b	0.04015	0.00234	0.27879	0.02283	0.01275	0.00018	253.8	14.5	249.7	18.1	256.8	3.7
15b	0.03747	0.00129	0.27695	0.07740	0.01230	0.00050	237.1	8.0	248.2	61.6	247.9	10.0
16b	0.04268	0.00234	0.29448	0.02286	0.01299	0.00015	269.5	14.5	262.1	17.9	261.5	3.0
17b	0.04111	0.00224	0.29280	0.02728	0.01283	0.00022	259.7	13.9	260.8	21.4	258.4	4.4
18b	0.04162	0.00209	0.29195	0.02501	0.01172	0.00030	262.9	12.9	260.1	19.7	236.3	6.0
Weighted average (Ma)							240.6		249.8		252.6	
Error 2σ (Ma)							4.6		7.6		2.2	
MSWD							2.4		1.3		9.8	

Discussion

The initial goal of our research was to determine the age of albite granite from Mt. Medvednica using zircon in order to refine the age frame of the Mesozoic processes in the study area. In addition, the recognition of the magmatic nature of epidote from the albite granite opens new possibilities for further petrogenetic considerations.

Nomenclature of the studied rock

The modal composition classification (Streckeisen 1974; corresponding graph is not shown here) defines the studied rock as an alkali feldspar (albite) granite. From a modal point of view, the albite granite plots in the alkaline granite field of this classification, which, taking into consideration texture and field characteristics, provides a few additional terms for naming the rock. The term "alkali feldspar granite" is only partially appropriate for a complete description of the rock, considering that albite with compositions up to An_5 should be added to the alkali feldspar mode. The term "aplite" is descriptively correct, but usually refers to the late crystallisation within a magmatic system. The term "oceanic plagiogranite" (Coleman & Peterman 1975) encompasses a wide spectrum of rocks associated with ophiolites. It is used for medium- to fine-grained rocks consisting predominantly of quartz and

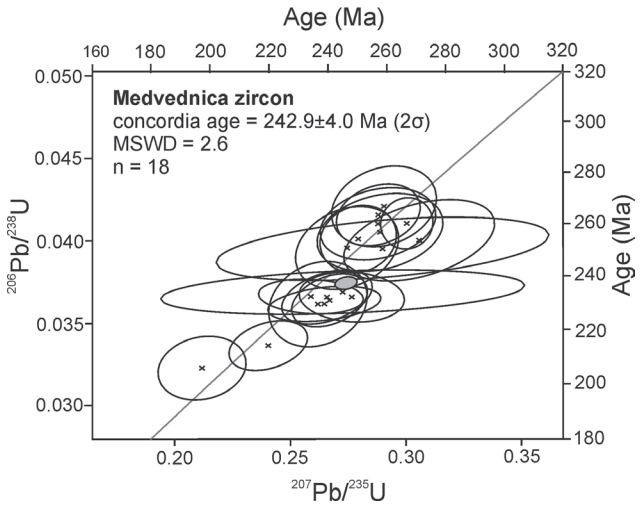

Fig. 5. U–Pb concordia diagram for zircon from the studied granite. Error ellipses relate to 1σ. Weighted average ages, 2σ, and MSWD values are given in Table 4.

zoned plagioclase ($An_{10–60}$) with less than 10% of ferromagnesian minerals (primary hornblende or pyroxene) that are characterised by granophyric intergrowth between quartz and plagioclase. This approximates our observations, even matching the chemistry of our sample (K, Rb, Na); however, the observed plagioclase is incompatible with the required one.

The granite from Mt. Medvednica, according to its mineral content, can be best classified as a leucocratic alkali feldspar (albite) granite. Among the mentioned possibilities, we prefer the historic term 'albite granite' for the studied rock, since it fulfils our observed features. This term has often been used to describe leucocratic rocks crystallising in late-orogenic to anorogenic granite complexes (Barboni & Bussy 2013).

Whole-rock geochemical characteristics

The whole-rock chemical composition should be primarily treated as a (fixed) chemical system for the thermodynamic modelling. Although one sample may not have the statistical significance needed for a detailed geochemical evaluation, the geochemical characteristics of the selected rock are notable enough for obtaining a general image of the geotectonic setting and description of the processes involved.

The chemical composition of XGO2 is governed by relatively moderate SiO_2, as well as high Al_2O_3 and Na_2O contents. The minor and trace elements correspond well with the granite signature characterised by the high contents of high field-strength (Y, Nb, Zr, Ga, Ta, U and Th) and large ion lithophile elements. The positive anomalies with respect to the primitive mantle according to Sun & McDonough (1989), which are visible for K, Pb, and Zr, as well as the negative anomalies for Rb, Nb, P and Ti (Fig. 3), imply the contribution of material from the continental crust to the melt that crystallised to albite granite.

The chondrite-normalised pattern of REE does not show the tetrad-effect (McLennan 1994), but exhibits a CHArge and RAdius Controlled (CHARAC) distribution, implying the absence of a significant amount of H_2O dissolved in the melt. The melt can be considered originally relatively dry, however, due to the presence of water-bearing magmatic minerals (amphibole(?), mica, epidote), it must have been enriched with H_2O in the required amount at some early point of the magmatic evolution.

Some authors attribute the occasional Na-rich character of A-type granites to post-magmatic metasomatic processes either by a pervasive infiltration of a fluid with a high Na/(Na+K) ratio or by a late exsolution of the magmatic fluid (e.g., Černý 1991; Kaur et al. 2006, 2012; Barboni & Bussy 2013 and references therein). The mineral chemistry and elemental geochemistry support the sheer magmatic origin of the albite granite from Mt. Medvednica, when taking into consideration the rationale of Barboni & Bussy (2013) as follows: (1) Textures of the albite granite, as well as the composition of minerals (epidote, zircon), are consistent with a magmatic origin. (2) Albite occurs as euhedral crystals (Fig. 2a, b) that grew in a cooling magma, whereas post-magmatic processes would form anhedral and/or interstitial grains. (3) Zircon usually shows traces of dissolution in contact with Na-rich hydrous fluids (spongy textures with mosaic zoning and pervasive recrystallisation, Rubatto et al. 2008), which was not observed in the studied albite granite. (4) Metasomatic processes affecting granites usually produce typical minerals, such as topaz or lepidolite. However, none of these minerals occur in the albite granite. (5) According to Wedepohl (1978), Nb is highly enriched during metasomatic albitisation. Such enrichment is not recorded by the albite granite (Nb=7.2 ppm; Table 1). (6) Post-magmatic metasomatism leads to a drastic increase in the contents of Rb, Ga, Li, and U (due to the recrystallisation of mica), while the contents of Eu, Sr, Ba (due to albitisation), and light REE (leaching of accessory phases) decrease. However, the albite granite displays relatively low contents of Rb (16.3 ppm), Ga (17.1 ppm), U (0.9 ppm), Eu (1.04 ppm), Sr (226 ppm, which could be ascribed to the secondary calcite too), Ba (362 ppm), and light REE (53 ppm).

Constraints from mineralogy

Zircon

Zircon grains are included in plagioclase and occasionally comprise their own inclusions. According to the zircon analyses (Table 3), these inclusions can be tentatively ascribed to a (Fe)-Ti-phase (?) and apatite. The morphology of zircon in the studied sample is typical for its crystallisation in a magma derived from melting in the lower crust (and upper mantle) at constant temperature (Pupin 1980; Pupin & Turco 1972). The positive Ce and negative Eu anomalies of the zircon chondrite-normalised patterns of REE provide evidence for the potential oxidation of the magma, corroborated by the high contents of REE, characteristic elemental ratios (see Fig. 3b),

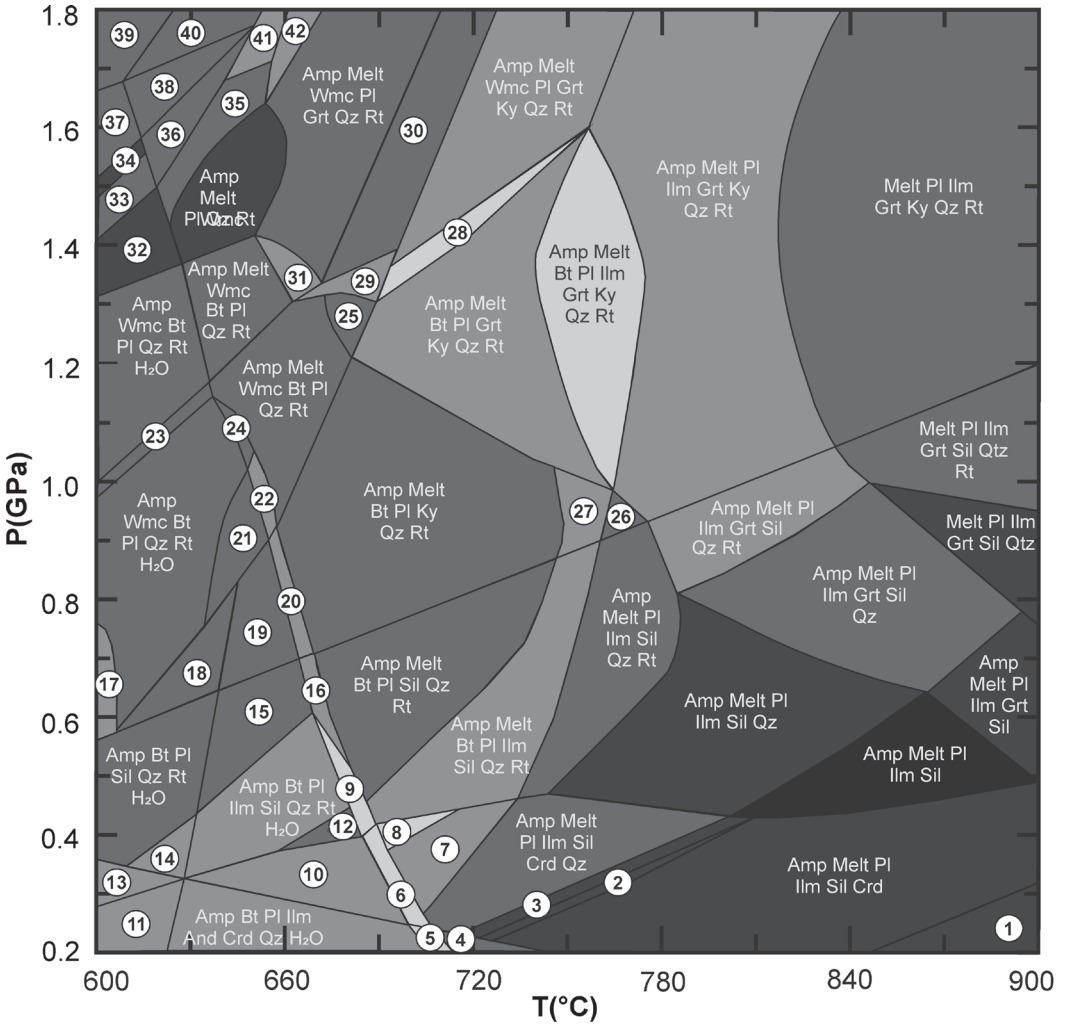

1 Amp Melt Pl Ilm Crd Hc
2 Amp Melt Pl Ilm Sil Crd
3 Amp Melt Pl Ilm Sil Crd
4 Amp Melt Pl Ilm And Crd H_2O
5 Amp Melt Bt Pl Ilm And Crd Qz H_2O
6 Amp Melt Bt Pl Ilm Sil Crd Qz H_2O
7 Amp Melt Bt Pl Ilm Sil Crd Qz
8 Amp Melt Bt Pl Ilm Sil Crd Qz Rt
9 Amp Melt Bt Pl Ilm Sil Qz Rt H_2O
10 Amp Bt Pl Ilm Sil Crd Qz H_2O
11 Amp Bt Pl Ilm And Crd Qz H_2O
12 Amp Bt Pl Ilm Sil Qz H_2O
13 Amp Bt Pl Ilm And Qz Rt H_2O
14 Amp Bt Pl Ilm Sil Qz Rt H_2O
15 Amp Bt Pl Sil Qz Rt H_2O
16 Amp Melt Bt Pl Sil Qz Rt H_2O
17 Amp Chl Wmc Bt Pl Qz Rt H_2O
18 Amp Bt Pl Ky Qz Rt H_2O
19 Amp Bt Pl Ky Qz Rt H_2O
20 Amp Melt Bt Pl Ky Qz Rt H_2O
21 Amp Wmc Bt Pl Qz Rt H_2O
22 Amp Melt Wmc Bt Pl Qz Rt H_2O
23 Amp Wmc Bt Pl Qz Rt H_2O
24 Amp Wmc Bt Pl Qz Rt H_2O
25 Amp Wmc Bt Pl Grt Qz Rt
26 Amp Melt Pl Ilm Ky Qz Rt
27 Amp Melt Bt Pl Ilm Ky Qz Rt
28 Amp Melt Wmc Bt Pl Grt Ky Qz Rt
29 Amp Melt Wmc Bt Pl Grt Qz Rt
30 Amp Melt Wmc Pl Grt Qz Rt
31 Amp Melt Wmc Bt Grt Pl Qz Rt
32 Amp Wmc Pl Qz Rt H_2O
33 Amp Wmc Spn Pl Qz Rt H_2O
34 Amp Wmc Spn Pl Qz H_2O
35 Amph Melt Ep Wmc Pl Qz Rt
36 Amp Melt Wmc Spn Pl Qz Rt
37 Amp Ep Wmc Spn Pl Qz H_2O
38 Amp Melt Ep Wmc Spn Pl Qz
39 Amp Ep Wmc Spn Jd Qz H_2O
40 Amp Melt Ep Wmc Spn Jd Qz
41 Amp Melt Ep Wmc Zo Pl Qz Rt
42 Amp Melt Ep Wmc Grt Pl Qz Rt

Fig. 6. P–T pseudo-section for the albite granite from Mt. Medvednica calculated with the PERPLE_X software in the Na–Ca–K–Fe–Mg–Al–Si–Ti–H–O system using a slightly modified whole-rock composition (in wt.%): Na_2O=5.779, CaO=1.213, K_2O=1.190, FeO=2.966, MgO=1.874, Al_2O_3=17.539, SiO_2=65.775, H_2O=3.000, TiO_2=0.632, O_2=0.033. For calculation details see the text; CaO was reduced for Ca bonded to calcite and apatite. The grey tones of the assemblage fields indicate the degree of variance of the corresponding assemblage (the darker the tone, the higher the variance). A few small P–T fields are not assigned to a mineral assemblage. Abbreviations of phases are from Whitney & Evans (2010).

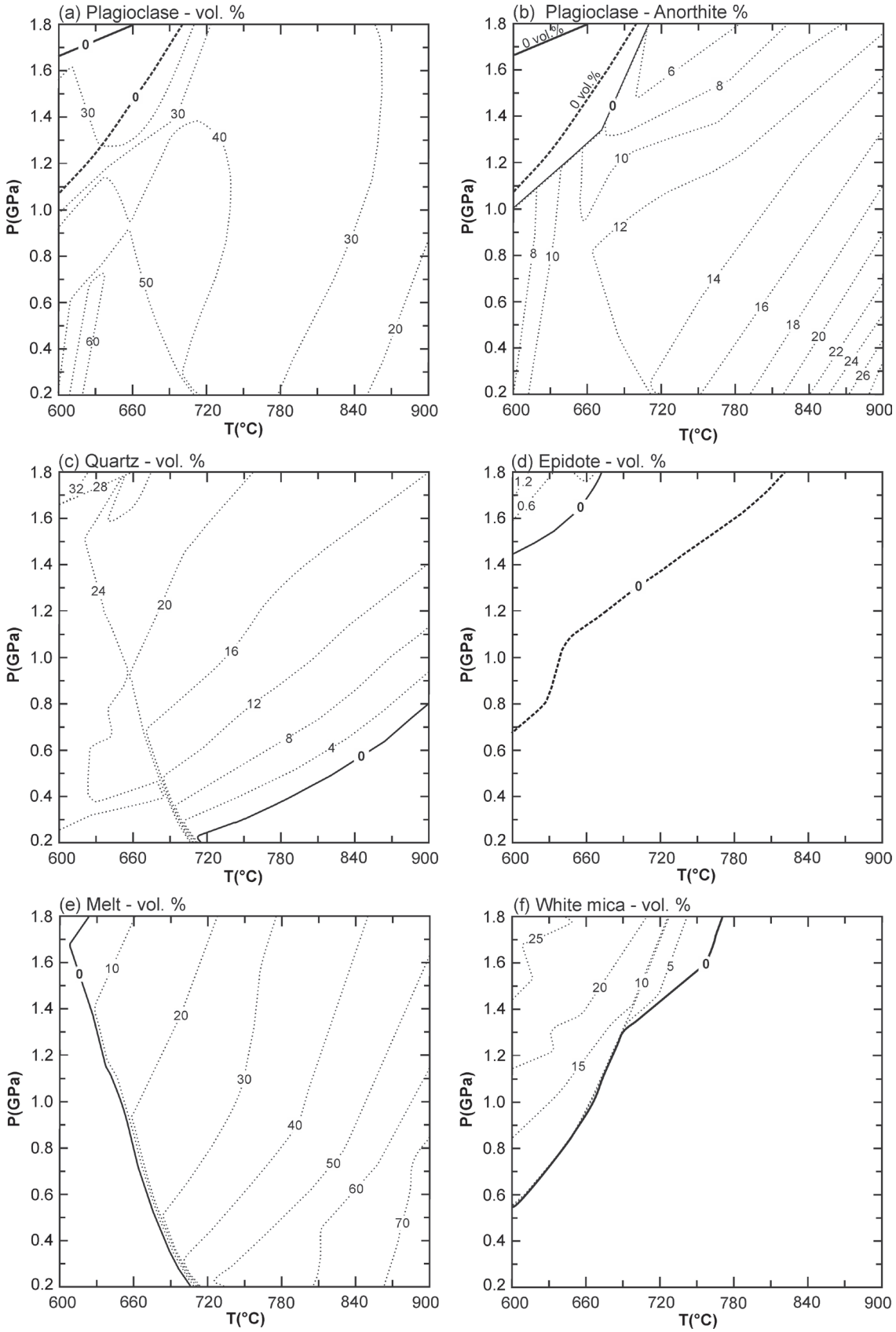

Fig. 7. Outlined P–T occurrences and modal contents (isomodes in vol.%) of the following mineral phases: **a** — plagioclase, **b** — An content of plagioclase, **c** — quartz, **d** — epidote, **e** — melt, **f** — white mica. Diagrams are related to the P–T pseudo-section in Fig. 6. Dashed lines in (a), (b) and (d) represent plagioclase and epidote in/out lines calculated with maximum (non-reduced for calcite) CaO in the system.

and the occurrence of magmatic epidote. The geochemical trends shown in Fig. 3a, b point to unaltered zircon crystallised from a magma (Belousova et al. 2002) formed by melting of crustal material (Hoskin & Ireland 2000). On the contrary, the zircon Zr/Hf ratio (48 compared to 37 in the whole-rock) indicates a mantle-derived dry (unsaturated) melt (Erdmann et al. 2013; Breiter & Škoda 2017). Such a dry magma likely incorporated a certain amount of H_2O at some point of the early magmatic evolution in order to enable the crystallisation of epidote and other H_2O-bearing minerals. The Th/U ratio (mean 3.77), being larger than 0.5, is also typical for igneous zircon (Hoskin & Schaltegger 2003; Kirkland et al. 2015). According to its chemical composition, zircon represents an early-stage mineral corroborated by its inclusion in plagioclase, another early-stage mineral.

The early-stage zircon, characterised by colourless and highly transparent crystals, usually forms in a deep magma chamber at a relatively high and constant temperature (Wang et al. 2010; Kirkland et al. 2015), which is compatible with the observed morphology of zircon grains (Pupin 1980). This is further corroborated by relatively low Hf concentrations in the studied zircon (HfO_2=0.71–1.65 wt. %, mean 1.24 wt. %), compared to values around 1.85 wt. % HfO_2, which are characteristic for late-stage zircon in general (Wang et al. 2010).

The zircon saturation temperature provides information of the minimum temperature of a granitic melt lacking inherited zircon (Miller et al. 2003). The calibration according to Watson & Harrison (1983) gives a temperature of 775 °C, similar to the Ti-in-zircon temperature (mean 785 °C) after Watson et al. (2006). Such elevated temperatures are considered characteristic of zircon crystallisation from magma with a source in the lower crust.

Epidote

Textural criteria (Schmidt & Poli 2004) were used to distinguish magmatic epidote from secondary epidote, as well as clinozoisite that are also present in the rock. The following petrographic features indicate epidote as magmatic mineral: (1) epidote formed after a Fe-Mg phase (hornblende?), but before or contemporaneously with biotite; (2) the corresponding texture resembles a typically magmatic (ophitic) one (Fig. 2a, b); (3) euhedral to subhedral epidote crystals show prismatic or hexagonal shapes (Fig. 2c, e–g); (4) a mineralogical association with a (primary) amphibole was reported by Majer & Majer (1974) from the locality where XGO2 was taken; (5) epidote grains contain allanite-rich cores; (6) epidote is embedded as single euhedral crystals in the quartz–feldspar matrix, which shows graphic intergrowths (Fig. 2d); and (7) embayed contacts of epidote with the quartzofeldspathic matrix were found (Fig. 2c, e–g). Both primary magmatic epidote and secondary clinozoisite occur together.

In the first report on this granite, Majer & Majer (1974) claimed that epidote is exclusively of secondary nature. Although the unequivocal identification of magmatic epidote is difficult, especially due to alteration processes and the inability to obtain fresh samples, further compositional criteria (ps=25–35, TiO_2 up to 0.14 wt. %; Liou 1973; Zen & Hammarstrom 1984; Keane & Morrison 1997; Schmidt & Poli 2004; Sial et al. 2008) point to magmatic epidote, which excludes a shallow crystallisation level for granodioritic to tonalitic magmas (e.g., Schmidt & Poli 2004). This type of epidote is relatively abundant (~1 vol. %) for the minor components in the studied rock. Subordinately, epidote also occurs as a post-magmatic phase, forming irregular grains that are preferentially associated with the altered plagioclase (Fig. 2d, e).

Epidote is stable above the wet granite solidus in the pressure range 0.5–3.0 GPa (Schmidt & Poli 2004). A relatively narrow temperature interval of epidote + melt occurs. Zen & Hammarstrom (1984) suggested that epidote indicates a minimum intrusive pressure of ~0.5–0.6 GPa or forms at pressures of

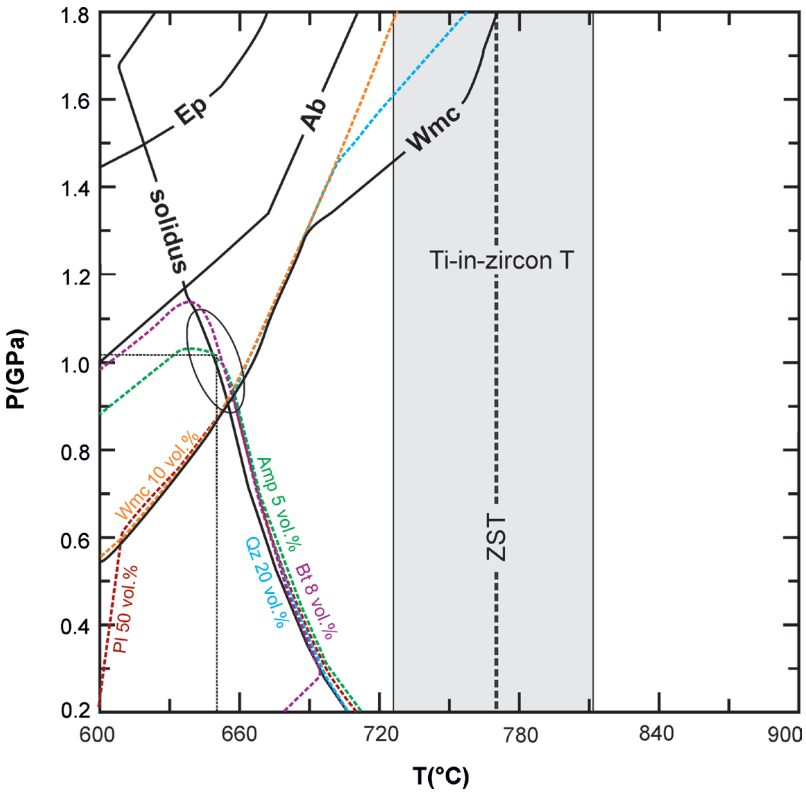

Fig. 8. Intersections of relevant isomodes for observed minerals offer the possibility of final crystallisation at about P=1.0 GPa, T=650 °C. P–T positions of fields for specific minerals and melt are constructed with 3 wt. % H_2O as in Fig. 6. Temperatures estimated on the basis of zircon saturation (ZST) according to Watson & Harrison (1983) and Ti-in-zircon from Watson et al. (2006) are marked.

0.3–0.7 GPa at suitable bulk composition and oxygen fugacity. Nevertheless, the minimum pressure for epidote crystallisation may vary (Schmidt & Poli 2004). Based on the intersection of the solidus curve with that of epidote, Liou (1973) and Crawford & Hollister (1982) proposed that in H_2O-saturated granitic melts, epidote requires a minimum crystallisation pressure of ~0.6 GPa. In granodioritic and tonalitic magmas, epidote is stable at pressures between 0.8 and 1.0 GPa at temperatures near the solidus curve (Liou 1973; Schmidt & Thompson 1996).

The crystallisation sequence of minerals (amphibole → epidote → plagioclase → biotite → quartz) is sensitive to pressure conditions (Schmidt & Poli 2004) and implies pressures above 1.0 GPa. The observed sequence and the P–T fields of epidote and plagioclase in the calculated pseudo-section (Fig. 7d, see also the dashed lines that represent these fields for the bulk rock without CaO reduction) show that epidote crystallisation fits the aforementioned pressure around 1.0 GPa. The P–T pseudo-section calculations for bulk-rock compositions with less H_2O down to 0.5 wt.%, which are more typical in the deeper crust, verify the position of the solidus, as well as epidote- and white mica (phengite)-in curves at high pressures. However, on the basis of the CO_2 determination of the bulk rock, a weaker reduction of CaO than reported in section "Analytical methods: Geothermobarometry", which is assumed to be bound to secondary calcite, would shift the lower pressure boundary of epidote and plagioclase to lower pressures. For example, a maximum CaO content of 4.46 wt.% in the original dry magma would lead to a reduction of the lower pressure limit of epidote to 0.7 GPa at a temperature of 600 °C (1.1 GPa at 660 °C). A similar effect can be predicted for epidote containing allanite component. Nevertheless, primary epidote challenges a shallow intrusion, which is a possible scenario for the Mt. Medvednica granite because of the surrounding low-grade rocks. Thus, epidote grains should have been protected by any means to prevent their reaction with melt and dissolution. Sial et al. (2008) suggested that fast upward magma transport increases the chance of epidote survival. Therefore, partially-corroded (embayed) epidote from the studied granite suggests a rapid magma ascent to preserve this mineral. This could be the case for many epidote-bearing granites worldwide (e.g., da Silva et al. 2020). The occurrence of zoned plagioclase and a quartz-feldspar matrix with graphic intergrowths (Fig. 2) are also in favour of a fast magma ascent. Since the present geological surrounding of the albite granite is made of clastic sedimentary rocks, a final tectonic emplacement from the intrusion level must also be taken into account.

White mica

Textural criteria point to two generations of white mica (Wmc1 and Wmc2, see above). If the larger crystals are considered to be a primary magmatic mineral, P–T conditions in the low-T and high-P part of the calculated pseudo-section would result (Figs. 6, 7f). The Si contents in potassic white mica, which usually crystallise late in a granitic melt, can, for example, be used to determine the intrusion level of this melt (Massonne et al. 2010). Following the graph published in the work of Massonne & Szpurka (1997, their figure 7), the Si content of 6.7 apfu and a solidus temperature of 650 °C indicate a pressure of 1.1 GPa. However, in the absence of K-feldspar, this pressure could also be somewhat lower (see the discussion in Liu & Massonne 2022). The P–T conditions of 650 °C and 1.1 GPa or somewhat lower are compatible with the crystallisation of epidote at high pressure (see the discussion in the previous section), which challenges a shallow intrusion level again. One alternative is the secondary formation of phengite. After complete crystallisation of the melt, an isobaric cooling to the temperatures of the surrounding metasediments can be expected. The potassic white mica forming at such subsolidus conditions becomes increasingly richer in Si with falling temperatures. For instance, phengite with 6.7 Si apfu could point to a pressure of 0.4 GPa (ca. 15 km of Earth's depth) only at temperatures of 400 °C lacking the K-feldspar provided.

Chlorite

Chlorite found in the studied rock cannot be a primary magmatic phase by its textural and assemblage characteristics. The leafy aggregates dominated by chlorite and containing minor opaque minerals (ilmenite, Fig. 2h) imply a transformation reaction of biotite to chlorite. The Ti previously in biotite is accommodated in ilmenite.

Amphibole

In our thin sections, we did not find amphibole that occurs in the P–T pseudo-section (Fig. 6, Supplementary Fig. S1b), and it reaches about 5 vol.% at the P–T conditions derived from primary phengite, although amphibole was reported by Majer & Majer (1974). We offer three explanations for the lacking amphibole: (1) it was decomposed to another mineral (such as chlorite), (2) the pseudo-section calculation led to amphibole as the phase that accommodates Ca, which is, however, in secondary calcite (overestimation of Ca in the bulk-rock composition of Table 1, see above) and (3) the used solid-solution model of amphibole is not appropriate (see the discussion in Massonne & Li 2022).

Regional geodynamic context

After termination of the subduction of the Palaeotethys Ocean below the European margin of Laurasia, the area of today's External Dinarides was positioned at the western rim of this ocean (Pamić et al. 2002; Schmid et al. 2008, 2020). A relatively calm period followed until the Middle Triassic, characterised by intensive tectonic movements related to the initial rifting and opening of the western branch of the Tethys Ocean (Neotethys). Such a rift-related geotectonic framework was accompanied by intense magmatic activity leading to thinned continental crust (Fig. 9).

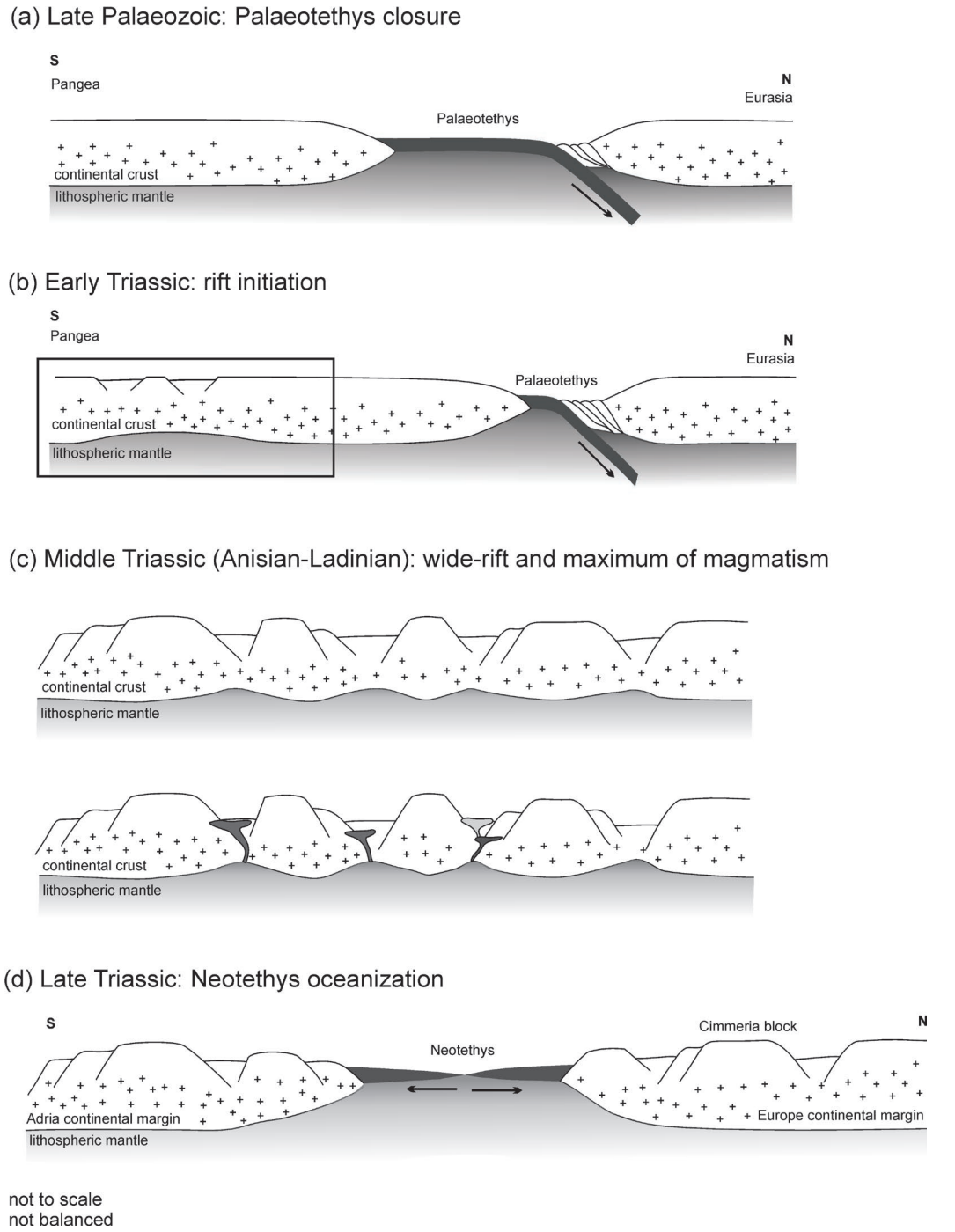

Fig. 9. Plausible geodynamic scenario for the investigated area at the turn of the Palaeozoic to the Mesozoic. **a** — Late Palaeozoic closure of the Palaeotethys with northward movement of Pangaea toward Eurasia. **b** — Lower Triassic rift initiation at the marginal parts of Pangaea. The boxed area is enlarged in (c) and (d). **c** — Formation of a "wide rift" in the Middle Triassic and maximum of magmatic activity during the Anisian–Ladinian; beginning of the Neotethys formation. **d** — Late Triassic: further oceanisation and widening of the Neotethys Ocean.

The first significant magmatic activity in the western Neotethys, calc-alkaline volcanism, occurred at the beginning of the Middle Triassic with a peak at the Anisian–Ladinian boundary in the Dinarides (e.g., Pamić 1984; Smirčić et al. 2018, 2020). Accompanied continental extension usually results in one of two types of rifting, leading to a "narrow" or "wide" rift (Buck 1991, 2015; Brun 1999; Brun et al. 2018). In wide rifts, continental thinning occurs over an area much wider than the thickness of the lithosphere (Buck 1991), whereas narrow rifts are no wider than the thickness of the continental lithosphere.

The occurrence of albite granite in the Mt. Medvednica area supports the "wide-rift" model (Buck 1991; Deng et al. 2020), which can lead to the surface exposure of acidic plutons and

their surrounding crustal rocks (Wernicke 1992). Moreover, the "wide rift" is recognised as a consequence of extension and thinning of the continental lithosphere (Buck 1991). Further fragmentation and disintegration of the continental crust in the Middle Triassic resulted in subsiding blocks discernable by various deep- and shallow-marine environments and the exposition of some of the blocks to weathering above sea level (e.g., Smirčić et al. 2018, 2020). Consequently, these events led to the onset of 'oceanisation'; i.e., extension of the Neotethys Ocean.

The Middle to Late Triassic magmatism has long been known to be widespread in the central part of the Southern Alps, as well as in the Dinaridic–Hellenic belt (e.g., Pamić 1984; Obenholzner 1991; Jelaska et al. 2003; Pamić & Balen 2005) and has been reported from the Western Carpathians as well (e.g., Putiš et al. 2000). However, the details of the igneous processes and the connection to the mid-Triassic geodynamic evolution in the areas of the Southern Alps, Dinarides–Hellenides, and Carpathians are still strongly debated (for a summary of different opinions regarding them, see Slovenec et al. 2020). The duration of igneous processes, the exact time scale, the boundaries between the different products of magmatic activity, as well as a unified geodynamic evolution have not been well-constrained yet, mainly due to irregularly-distributed occurrences, a lack of high-precision isotopic age determinations, different scientific approaches, and a rather complicated geological situation during the Alpine orogeny.

The magmatic activity in the Middle Triassic with explosive acid volcanism in the wider Alpine–Dinaridic–Carpathian realm is characterised by volcanic ash layers. These layers are intercalated with Middle Triassic sediments called *pietra verde* (von Richthofen 1860). The main purpose of studying these volcanic ash layers was to correlate the obtained ages with the biostratigraphy. These ages are mostly centred between 241 and 238 Ma (Neubauer et al. 2014; Dunkl et al. 2019) and thus compatible with the determined U–Pb zircon age here (243 Ma). However, in addition to *pietra verde,* the South Alpine–Dinaridic–Carpathian igneous activity in the Middle Triassic produced highly variable intrusive-volcanic assemblages.

In the area of the westernmost Tethys in the Southern Alps (northern Italy), the Middle to early Late Triassic (~243–235 Ma) is characterised by a diffuse igneous activity comprising volcanoclastic deposits, basaltic lava flows, and intrusive complexes. Contemporaneous igneous products can be traced eastwards to Austria and the Dinarides for a total length of ~450 km (Lustrino et al. 2019). A comprehensive high-precision U–Pb zircon geochronology dataset for the major intrusive complexes and several volcanic ash layers for the Middle Triassic magmatism in the Southern Alps was presented by Storck et al. (2019). Magmatic activity in the Southern Alps started with silicic eruptions between 242.65±0.04 and 238.65±0.04 Ma and were followed by mafic to intermediate intrusions (238.19±0.06 to 238.08±0.09 Ma). The youngest products in the Southern Alps are silicic tuffs from late Ladinian to early Carnian sequences (237.68±0.05 to 237.58±0.04 Ma). Thus, a short duration (5.1±0.1 million years, Storck et al. 2019) of Middle Triassic magmatism in the Southern Alps occurred.

The U–Pb ages indicate a nearly contemporaneous beginning of volcanic activity within the Transdanubian Range toward the Western Carpathians. The volcanoclastic formations in the Transdanubian Range record two major periods of volcanic activity according to zircon dated at 238.2±0.9 Ma and 229.4±1.1 Ma (Dunkl et al. 2019). The Triassic volcanic sources in the Western Carpathians yielded zircon ages of (1) 238.6±1.4 Ma for the crystallization of A-type granite (Putiš et al. 2000) and (2) 221.2±1.6 Ma, which demonstrates the upper limit of the Carnian stage in the Alpine–Carpathian realm (Kohút et al. 2018) marking a significant lithological and climate change known as the "Carnian Crisis".

De Min et al. (2020) summarised in detail the onset of the Triassic magmatism in southern Europe. This magmatism was triggered by the extensional and trans-tensional tectonics related to the large-scale rifting system, which initiated the opening of oceanic domains and the break-up of the continental crust (Pangaea). According to such a scenario, magmatism took place as a consequence of mantle upwelling due to the heat accumulated beneath the continental crust. Storck et al. (2020) performed thermal simulations for the peak event in the Middle Triassic magmatic province in the Southern Alps (northern Italy). The results presented suggest that upwelling asthenosphere indeed explains the thinning of the crust and the subsequent "rifting" that brings hot material up from the mantle. These thermal simulations provide an explanation and theoretical background for the hot zone in the lower crustal and the peak of magmatic activity in the Southern Alps, culminating in major intrusive bodies (Predazzo and Monzoni). This included voluminous pillow basalts, even for the age-anchored Hf isotopic shift from crustal-like signature to more sub-continental lithospheric mantle signatures.

The thickness of the Triassic crust along the segment of the Pangaea continental margin discussed here is estimated on the basis of the empirical relationship between the Sr/Y ratio (9.25) and crustal thickness D_M according to Hu et al. (2017; D_M=0.67 Sr/Y+28.21). We obtained a ~34 km thick crust (~1.0 GPa lithostatic pressure at the crust-mantle boundary). Timing, whole rock, and mineral geochemistry with lower crustal signatures, as well as the invoked processes of thinning of the inherited thick(er) continental crust in our scenario (Fig. 9) fit well with such a large-scale view and thermal simulations.

Our zircon crystallisation age of 242.9±4.0 Ma (2σ) coincides with the peak of magmatic activities in the Dinarides in the Middle Triassic (Anisian–Ladinian) (e.g., Pamić 1984; Smirčić et al. 2018, 2020), but also in the Southern Alps and Western Carpathians. According to the above discussion, we suggest that the studied albite granite indicates changes from a tectonically relatively calm period in the Lower Triassic to the opening of the western branch of the Neotethys Ocean (Fig. 9). This scenario, which invokes a "wide rift", can

explain the ascent of epidote-bearing granitic magma. Viscosity is usually a key factor in the velocity of rising granitic magmas (Brown & Solar 1998; Giordano et al. 2008) and depends on the melt composition and particularly SiO_2 content, temperature, and H_2O content (Cruden & Weinberg 2018). However, the thermal and mechanical weakening of a former continental domain at a "wide-rift" margin might allow for relatively viscous acidic magmas to ascend.

Conclusions

Our petrological and geochronological study of an albite granite from Mt. Medvednica (Križevna Bukva), including thermodynamic modelling at supersolidus conditions, resulted in P–T conditions of about 1.0 GPa at ≥650 °C for the early crystallisation of minerals, such as epidote in granitic (siliceous, metaluminous, and alkaline = high Na) melt. The $^{206}Pb/^{238}U$ versus $^{207}Pb/^{235}U$ concordia age determined on zircon is 242.9±4.0 Ma (2σ), which coincides with the Anisian–Ladinan boundary, i.e., the peak of the Triassic magmatic activity in the Dinarides, Southern Alps, and Western Carpathians. We interpret this age as representing the beginning of significant Middle Triassic fragmentation of the continental lithosphere and onset of oceanisation in the area. The proposed "wide-rift" model enables fast ascent of viscous acidic melts. This model is a consequence of extension and thinning of the continental lithosphere, followed by the subsequent broadening of the newly-formed Neotethys Ocean.

Acknowledgements: The authors are grateful to Ralf Schuster, Julian-Christopher Storck, and the editor Milan Kohút for their constructive comments during the review process. Financial support from the University of Zagreb (Potpora istraživanjima) is greatly appreciated.

References

Babić LJ., Hochuli P.A. & Zupanič J. 2002: The Jurassic ophiolitic mélange in the NE Dinarides: Dating, internal structure and geotectonic implications. *Eclogae Geologicae Helvetiae* 95, 263–275. https://doi.org/10.5169/seals-168959

Balen D. 2015: Zircon typology – application in geological research [Morfologija cirkona – primjena u geološkim istraživanjima]. In: Znanstveni skup Suvremena kristalografija u Hrvatskoj. *Hrvatska akademija znanosti i umjetnosti*, Zagreb, 123–134 (in Croatian).

Balen D., Schneider P., Massonne H.-J., Opitz J., Luptáková J., Putiš M. & Petrinec Z. 2020: The Late Cretaceous A-type alkali-feldspar granite from Mt. Požeška Gora (N Croatia): Potential marker of fast magma ascent in the Europe–Adria suture zone. *Geologica Charpathica* 71, 361–381. https://doi.org/10.31577/GeolCarp.71.4.5

Barboni M. & Bussy F. 2013: Petrogenesis of magmatic albite granites associated to cogenetic A-type granites: Na-rich residual melt extraction from a partially crystallized A-type granite mush. *Lithos* 177, 328–351. https://doi.org/10.1016/j.lithos.2013.07.005

Basch O. 1981: Basic Geological Map of Yugoslavia in scale 1:100,000, sheet Ivanić-Grad L33-81 [Osnovna geološka karta SFRJ M 1:100.000, list Ivanić-Grad L33-81]. *Geološki Institut Zagreb, Federal Geological Institute Beograd* (in Croatian).

Basch O. 1983: Basic Geological Map of Yugoslavia in scale 1:100,000, Explanatory notes for sheet Ivanić Grad (L 38-81) [Tumač za list Ivanić-Grad L 38-81]. *Geološki Institut Zagreb, Federal Geological Institute Beograd*, 1–61 (in Croatian).

Belak M. & Tibljaš D. 1998: Discovery of the blueschist in the Medvednica Mountain (Northern Croatia) and their significance for the interpretation of the geotectonic evolution of the area. *Geologia Croatica* 51, 27–32. https://doi.org/10.4154/GC.1998.05

Belak M., Pamić J., Kolar-Jurkovšek T., Pecskay Z. & Karan D. 1995: Alpine low-grade regional metamorphic complex of Mt. Medvednica (northwestern Croatia). In: Vlahović I., Velić I. & Šparica M. (Eds.): Proceedings of 1st Croatian Geological Congress Opatija october 18–21, 1995. *Institut za Geološka istraživanja*, Zagreb, 67–70 (in Croatian).

Belousova E.A., Walters S., Griffin W.L., O'Reilly S.Y. & Fisher N.I. 2002: Igneous zircon: trace element composition as an indicator of source rock type. *Contributions to Mineralogy and Petrology* 143, 602–622. https://doi.org/10.1007/s00410-002-0364-7

Boynton W.V. 1984: Geochemistry of the rare earth elements: meteorite studies. In: Henderson P. (Ed.): Rare earth element geochemistry. *Elsevier*, New York, 63–114.

Breiter K. & Škoda R. 2017: Zircon and whole-rock Zr/Hf ratios as markers of the evolution of granitic magmas: Examples from the Teplice caldera (Czech Republic/Germany). *Mineralogy and Petrology* 111, 435–457. https://doi.org/10.1007/s00710-017-0509-z

Brown M. & Solar G.S. 1998: Granite ascent and emplacement during contractional deformation in convergent orogens. *Journal of Structural Geology* 20, 1365–1393. https://doi.org/10.1016/S0191-8141(98)00074-1

Brun J.-P. 1999: Narrow rifts versus wide rifts: inferences for the mechanics of rifting from laboratory experiments. *Philosophical Transactions of the Royal Society of London, Series A: Mathematical, Physical and Engineering Sciences* 357, 695–712. https://doi.org/10.1098/rsta.1999.0349

Brun J.-P., Sokoutis D., Tirel C., Gueydan F., Van Den Driessche J. & Beslier M.O. 2018 : Crustal versus mantle core complexes. *Tectonophysics* 746, 22–45. https://doi.org/10.1016/j.tecto.2017.09.017

Buck W.R. 1991: Modes of continental lithospheric extension. *Journal of Geophysical Research* 96, 20161–20178. https://doi.org/10.1029/91JB01485

Buck W.R. 2015: The dynamics of continental breakup and extension. In: Schubert G. (Ed.): Treatise on Geophysics (second edition). *Elsevier*, Oxford, 325–379.

Černý P. 1991: Rare-element granitic pegmatites. Part 1. Anatomy and internal evolution of pegmatite deposits. *Geosciences Canada* 18, 49–67.

Coleman R.G. & Peterman Z.E. 1975: Oceanic plagiogranite. *Journal of Geophysical Research* 80, 1099–1108. https://doi.org/10.1029/JB080i008p01099

Connolly J.A.D. 1990: Multivariable phase-diagrams: an algorithm based on generalized thermodynamics. *American Journal of Science* 290, 666–718. https://doi.org/10.2475/ajs.290.6.666

Connolly J.A.D. 2005: Computation of phase equilibria by linear programming: A tool for geodynamic modeling and its application to subduction zone decarbonation. *Earth and Planetary Science Letters* 236, 524–541. https://doi.org/10.1016/j.epsl.2005.04.033

Connolly J.A.D. & Petrini K. 2002: An automated strategy for calculation of phase diagram sections and retrieval of rock properties as a function of physical conditions. *Journal of Metamorphic Geology* 20, 697–708.

Crawford M.L. & Hollister L.S. 1982: Contrast of metamorphic and structural histories across the Work Channel lineament, Coast Plutonic Complex, British Columbia. *Journal of Geophysical Research* 87, 3849–3860.

Croatian Geological Survey 2009: Geological map of the Republic of Croatia, M 1:300,000 [Geološka karta Republike Hrvatske]. *Croatian Geological Survey*, *Department of Geology*, Zagreb (in Croatian).

Cruden A.R. & Weinberg R.F. 2018: Mechanisms of Magma Transport and Storage in the Lower and Middle Crust-Magma Segregation, Ascent and Emplacement. In: Burchardt S. (Ed): Volcanic and igneous plumbing systems: Understanding magma transport, storage, and evolution in the earth's crust. *Elsevier*, Amsterdam, 13–53.

da Silva T.R., Ferreira V.P., de Lima M.M.C. & Sial A.N. 2020: Rapid magma ascent and formation of the Águas Belas–Canindé granitic batholith, NE Brazil: evidence of epidote dissolution and thermobarometry. *Brazilian Journal of Geology* 50. https://doi.org/10.1590/2317-4889202020190110

De Min A., Velicogna M., Ziberna L., Chiaradia M., Alberti A. & Marzoli A. 2020: Triassic magmatism in the European Southern Alps as an early phase of Pangea break-up. *Geological Magazine* 157, 1800–1822. https://doi.org/10.1017/S0016756820000084

Deng H., Ren J., Pang X., Rey P.F., McClay K.R., Watkinson I.M., Zheng J. & Luo P. 2020: South China Sea documents the transition from wide continental rift to continental break up. *Nature Communications* 11, 4583. https://doi.org/10.1038/s41467-020-18448-y

Dickinson W. & Gehrels G. 2003: U–Pb ages of detrital zircons from Permian and Jurassic eolian sandstones of the Colorado Plateau, USA: paleogeographic implications. *Sedimentary Geology* 163, 29–66. https://doi.org/10.1016/S0037-0738(03)00158-1

Dunkl I., Farics É., Józsa S., Lukács R., Haas J. & Budai T. 2019: Traces of Carnian volcanic activity in the Transdanubian Range, Hungary. *International Journal of Earth Sciences (Geologische Rundschau)* 108, 1451–1466. https://doi.org/10.1007/s00531-019-01714-w

Erdmann S., Wodicka N., Jackson S.E. & Corrigan D. 2013: Zircon textures and composition refractory recorders of magmatic volatile evolution? *Contributions to Mineralogy and Petrology* 165, 45–71. https://doi.org/10.1007/s00410-012-0791-z

Giordano D., Russell J.K. & Dingwell D.B. 2008: Viscosity of magmatic liquids: A model. *Earth and Planetary Science Letters* 271, 123–134. https://doi.org/10.1016/j.epsl.2008.03.038

Goričan Š., Halamić J., Grgasović T. & Kolar-Jurkovšek T. 2005: Stratigraphic evolution of Triassic arc-back arc system in northwestern Croatia. *Bulletin de la Societe Geologique de France* 176, 3–22.

Green E.C.R., White R.W., Diener J.F.A., Powell R., Holland T.J.B. & Palin R.M. 2016: Activity–composition relations for the calculation of partial melting equilibria in metabasic rocks. *Journal of Metamorphic Geology* 34, 845–869. https://doi.org/10.1111/jmg.12211

Halamić J. 1998: Lithostratigraphy of Jurassic and Cretaceous sediments with ophiolites from the Mts. Medvednica, Kalnik and Ivanščica. [Litostratigrafska kategorizacija jurskih i krednih sedimenata s ofiolitima Medvednice, Kalnika i Ivanščice]. *PhD Thesis*, *University of Zagreb*, 1–188 (in Croatian with English summary).

Holland T. & Powell R. 2003: Activity–composition relations for phases in petrological calculations: an asymmetric multicomponent formulation. *Contributions to Mineralogy and Petrology* 145, 492–501. https://doi.org/10.1007/s00410-003-0464-z

Holland T.J.B. & Powell R. 2011: An improved and extended internally consistent thermodynamic dataset for phases of petrological interest, involving a new equation of state for solids. *Journal of Metamorphic Geology* 29, 333–383. https://doi.org/10.1111/j.1525-1314.2010.00923.x

Holland T.J.B., Green E.C.R. & Powell R. 2018: Melting of Peridotites through to Granites: A Simple Thermodynamic Model in the System KNCFMASHTOCr. *Journal of Petrology* 59, 881–900. https://doi.org/10.1093/petrology/egy048

Hoskin P.W.O. & Ireland T.R. 2000: Rare earth element chemistry of zircon and its use as a provenance indicator. *Geology* 28, 627–630. https://doi.org/10.1130/0091-7613(2000)28<627:REECOZ>2.0.CO;2

Hoskin P.W.O. & Schaltegger U. 2003: The composition of zircon and igneous and metamorphic petrogenesis. *Reviews in Mineralogy and Geochemistry* 53, 27–62. https://doi.org/10.2113/0530027

Hu F., Ducea M.N., Liu S. & Chapman J.B. 2017: Quantifying Crustal Thickness in Continental Collisional Belts: Global Perspective and a Geologic Application. *Scientific Reports* 7, 7058. https://doi.org/10.1038/s41598-017-07849-7

Janoušek V., Farrow C.M. & Erban V. 2006: Interpretation of whole-rock geochemical data in igneous geochemistry: introducing Geochemical Data Toolkit (GCDkit). *Journal of Petrology* 47, 1255–1259. https://doi.org/10.1093/petrology/egl013

Jelaska V., Kolar-Jurkovšek T., Jurkovšek B. & Grušić I. 2003: Triassic beds in the basement of the Adriatic–Dinaric carbonate platform of Mt. Svilaja (Croatia). *Geologija* 46, 225–230.

Johannes W.J. 1978: Pressure comparing experiments with NaCl, AgCl, talc, and pyrophyllite assemblies in a piston cylinder apparatus. *Neues Jahrbuch Mineralogie Monatshefte*, 84–92.

Judik K., Árkai P., Horváth P., Dobosi G., Tibljaš D., Balen D., Tomljenović B. & Pamić J. 2004: Diagenesis and low-temperature metamorphism of Mt. Medvednica, Croatia: Mineral assemblages and phyllosilicate characteristics. *Acta geologica Hungarica* 47, 151–176. https://doi.org/10.1556/AGeol.47.2004.2-3.5

Judik K., Balogh K., Tibljaš D. & Árkai P. 2006: New age data on the low-temperature regional metamorphism of Mt. Medvednica (Croatia). *Acta geologica Hungarica* 49, 207–221. https://doi.org/10.1556/AGeol.49.2006.3.2

Kaur P., Chaudrih N., Okrush M. & Koepke J. 2006: Palaeoproterozoic A-type felsic magmatism in the Khetri Copper Belt, Rajasthan, northwestern India: petrologic and tectonic implications. *Mineralogy and Petrology* 87, 81–122. https://doi.org/10.1007/S00710-005-0118-0

Kaur P., Chaudhri N., Hofmann A.W., Raczek I., Okrusch M., Skora S. & Baumgartner L.P. 2012: Two-Stage, Extreme Albitization of A-type Granites from Rajasthan, NW India, *Journal of Petrology* 53, 919–948. https://doi.org/10.1093/petrology/egs003

Keane S.D. & Morrison J. 1997: Distinguishing magmatic from subsolidus epidote: laser probe oxygen isotope compositions. *Contributions to Mineralogy and Petrology* 126, 265–274.

Kirkland C.L., Smithies R.H., Taylor R.J.M., Evans N. & Mcdonald B. 2015: Zircon Th/U ratios in magmatic environs. *Lithos* 212–215, 397–414. https://doi.org/10.1016/j.lithos.2014.11.021

Kohút M., Hofmann M., Havrila M., Linnemann U. & Havrila J. 2018: Tracking an upper limit of the "Carnian Crisis" and/or Carnian stage in the Western Carpathians (Slovakia). *International Journal of Earth Sciences (Geologische Rundschau)*107, 321–335. https://doi.org/10.1007/s00531-017-1491-8

Liou J.G. 1973: Synthesis and stability relations of epidote, $Ca_2Al_2FeSi_3O_{12}(OH)$. *Journal of Petrology* 14, 381–413. https://doi.org/10.1093/petrology/14.3.381

Liu P. & Massonne H.-J. 2022: High-pressure granulite facies re-equilibration and zoisite-biotite dehydration melting during decompression of an ultrahigh-pressure garnet clinopyroxenite from the island of Fjørtoft, Norway. *Journal of Metamorphic Geology* 40, 887–918. https://doi.org/10.1111/jmg.12649

Lugović B., Šegvić B. & Altherr R. 2006: Petrology and tectonic significance of greenschists from the Medvednica Mts. (Sava Unit, NW Croatia). *Ofioliti* 31, 39–50.

Lugović B., Slovenec D., Halamić J. & Altherr R. 2007: Petrology, geochemistry and geotectonic affinity of the Mesozoic ultramafic rocks from the southwesternmost mid-Transdanubian zone in Croatia. *Geologica Carpathic*a 58, 511–530. https://doi.org/10.4154/GC.2015.03

Lustrino M., Abbas H., Agostini S., Caggiati M., Carminati E. & Gianolla P. 2019: Origin of Triassic magmatism of the Southern Alps (Italy): Constraints from geochemistry and Sr–Nd–Pb isotopic ratios. *Gondwana Research* 75, 218–238. https://doi.org/10.1016/j.gr.2019.04.011

Lužar-Oberiter B., Mikes T., Dunkl I., Babić Lj. & Von Eynatten H. 2012: Provenance of Cretaceous synorogenic sediments from the NW Dinarides (Croatia). *Swiss Journal of Geosciences* 105, 377–399. https://doi.org/10.1007/s00015-012-0107-3

Majer E. & Majer V. 1974: Pojave stijena spilit–keratofirske asocijacije u sjeveroistočnom dijelu Medvednice (Hrvatska, Jugoslavija) [Die Gesteine der Spilit–Keratophyr-Assoziation im nordöstlichen Teil des Medvednica-Gebirges (Kroatien, Jugoslawien)]. *Geološki vjesnik* 27, 189–198.

Massonne H.-J. 2012: Formation of amphibole and clinozoisite-epidote in eclogite owing to fluid infiltration during exhumation in a subduction channel. *Journal of Petrology* 53, 1969–1998. https://doi.org/10.1093/petrology/egs040

Massonne H.-J. & Li B. 2022: Eclogite with unusual atoll garnet from the southern Armorican Massif, France: pressure-temperature path and geodynamic implications. *Tectonophysics* 823, 229183. https://doi.org/10.1016/j.tecto.2021.229183

Massonne H.-J. & Szpurka Z. 1997: Thermodynamic properties of white micas on the basis of high-pressure experiments in the systems K_2O–MgO–Al_2O_3–SiO_2–H_2O and K_2O–FeO–Al_2O_3–SiO_2–H_2O. *Lithos* 41, 229–250. https://doi.org/10.1016/S0024-4937(97)82014-2

Massonne H.-J., Willner A.P. & Gerya T.V. 2007: Densities of psammopelitic rocks at elevated temperatures and high to ultrahigh pressure conditions: what are the geodynamic consequences? *Earth and Planetary Science Letters* 256, 12–27. https://doi.org/10.1016/j.epsl.2007.01.013

Massonne H.-J., Clarke D.B. & MacDonald M.A. 2010: Intrusion level of the Musquodoboit Batholith in Nova Scotia, Canada – a case study. *Zeitschrift fur Geologische Wissenschaften* 38, 181–194.

McLennan S.M. 1994: Rare earth element geochemistry and the "tetrad" effect. *Geochimica et Cosmochimica Acta* 58, 2025–2033. https://doi.org/10.1016/0016-7037(94)90282-8

Miller C.F., McDowell S.M. & Mapes R.W. 2003: Hot and cold granites? Implications of zircon saturation temperatures and preservation of inheritance. *Geology* 31, 529–532. https://doi.org/10.1130/0091-7613(2003)031<0529:HACGIO>2.0.CO;2

Neubauer F., Xiaoming L., Borojević Šoštarić S., Bianca H. & Yunpeng D. 2014: U–Pb zircon data of Middle–Upper Triassic magmatism in Southern Alps and NW Dinarides: Implications for the Southeast Mediterranean tectonics. In: Proceedings XX Congress of the Carpathian-Balkan Geological Association, Tirana, Albania. *Buletini i Shkencave Gjeologjike* 1/2014, Special Issue.

Obenholzner J.H. 1991: Triassic volcanogenic sediments from the Southern Alps (Italy, Austria, Yugoslavia) – a contribution to the "Pietra verde" problem. *Sedimentary Geology* 74, 157–171. https://doi.org/10.1016/0037-0738(91)90038-F

Paces J.B. & Miller J.D. 1993: Precise U–Pb ages of Duluth Complex and related mafic intrusions, northeastern Minnesota: geochronological insights into physical, petrogenetic, paleomagnetic and tectonomagmatic processes associated with the 1.1 Ga midcontinent rift system. *Journal of Geophysical Research* 98, 13997–14013. https://doi.org/10.1029/93JB01159

Palinkaš L., Bermanec V., Borojević Šoštarić S., Kolar-Jurkovšek T., Strmić Palinkaš S., Molnar F. & Kniewald G. 2008: Volcanic facies analysis of a subaqueous basalt lava-flow complex at Hruškovec, NW Croatia - evidence of advanced rifting in the Tethyan domain. *Journal of Volcanology and Geothermal Research* 178, 644–656. https://doi.org/10.1016/j.jvolgeores.2008.06.037

Pamić J. 1984: Triassic magmatism of the Dinarides in Yugoslavia. *Tectonophysics* 109, 273–307. https://doi.org/10.1016/0040-1951(84)90145-8

Pamić J. & Balen D. 2005: Interaction between permo-Triassic rifting, magmatism and initiation of the Adriatic-Dinaridic carbonate platform (ADCP). *Acta Geologica Hungarica* 48, 181–204. https://doi.org/10.1556/ageol.48.2005.2.6

Pamić J. & Tomljenović B. 1998: Basic geological data on the Croatian part of the Mid-Transdanubian Zone as exemplified by Mt. Medvednica located along the Zagreb-Zemplen Fault Zone. *Acta Geologica Hungarica* 41, 389–400.

Pamić J., Tomljenović B. & Balen D. 2002: Geodynamic and petrogenetic evolution of Alpine ophiolites from the central and NW Dinarides: an overview. *Lithos* 65, 113–142. https://doi.org/10.1016/S0024-4937(02)00162-7

Pupin J.P. 1980: Zircon and granite petrology. *Contributions to Mineralogy and Petrology* 73, 207–220.

Pupin J.P. & Turco G. 1972: Une typologie originale du zircon accessoire. *Bulletin de la Société française de Minéralogie et de Cristallographie* 95, 348–359.

Putiš M., Kotov A.B., Uher P., Salnikova J.B. & Korikovsky S.P. 2000: Triassic age of the Hrončok Pre-Orogenic A-type granite related to continental rifting: a new result of U–Pb isotope dating (Western Carpathians). *Geologica Carpathica* 51, 59–66.

Rubatto D., Müntener O., Barhoorn A. & Gregory C. 2008: Dissolution–reprecipitation of zircon at low-temperature, high-pressure conditions (Lanzo Massif; Italy). *American Mineralogist* 93, 1519–1529. https://doi.org/10.2138/am.2008.2874

Schmid S.M., Bernoulli D., Fügenschuh B., Matenco L., Schefer S., Schuster R., Tischler M. & Ustaszewski K. 2008: The Alps–Carpathians–Dinarides connection: a compilation of tectonic units. *Swiss Journal of Geosciences* 101, 139–183. https://doi.org/10.1007/s00015-008-1247-3

Schmid S.M., Fügenschuh B., Kounov A., Maţenco L., Nievergelt P., Oberhänsli R., Pleuger J., Schefer S., Schuster R., Tomljenović B., Ustaszewski K. & Van Hinsbergen D.J.J. 2020: Tectonic units of the Alpine collision zone between Eastern Alps and western Turkey. *Gondwana Research* 78, 308–374. https://doi.org/10.1016/j.gr.2019.07.005

Schmidt M.W. & Poli S. 2004: Magmatic epidote. *Reviews in Mineralogy and Geochemistry* 56, 399–430. https://doi.org/10.2138/gsrmg.56.1.399

Schmidt M.W. & Thompson A.B. 1996: Epidote in calc-alkaline magmas: An experimental study of stability, phase relationships, and the role of epidote in magmatic evolution. *American Mineralogist* 81, 462–474. https://doi.org/10.2138/am-1996-3-420

Shaulis B., Lapen T.J. & Toms A. 2010: Signal linearity of an extended range pulse counting detector: Applications to accurate and precise U–Pb dating of zircon by laser ablation quadrupole ICPMS. *Geochemistry, Geophysics, Geosystems* 11, Q0AA11. https://doi.org/10.1029/2010GC003198

Sial A.N., Vasconcelos P.M., Ferreira V.P., Pessoa R.R., Brasilino R.G. & Morais Neto J.M. 2008: Geochronological and mineralogical constraints on depth of emplacement and ascension rates of epidote-bearing magmas from northeastern Brazil. *Lithos* 105, 225–238. https://doi.org/10.1016/j.lithos.2008.04.002

Sláma J., Kosler J., Condon D.J., Crowley J.L., Gerdes A., Hanchar J.M., Horstwood M.S.A., Morris G.A., Nasdala L., Norberg N., Schaltegger U., Schoene N., Tubrett M.N. & Whitehouse M.J. 2008: Plesovice zircon – a new natural reference material for U–Pb and Hf isotopic microanalysis. *Chemical Geology* 249, 1–35. https://doi.org/10.1016/j.chemgeo.2007.11.005

Slovenec D. & Lugović B. 2012: Evidence of the spreading culmination in the eastern Tethyan Repno oceanic domain, assessed by the petrology and geochemistry of N-MORB extrusive rocks from the Mt. Medvednica ophiolite mélange (NW Croatia). *Geologica Croatica* 65, 435–446. https://doi.org/10.4154/gc.2012.32

Slovenec D., Lugović B., Halamić J. & Altherr R. 2007: Petrology, geochemistry and tectonic significance of mesozoic ultramafic rocks from the Zagorje-Mid-Transdanubian Zone in Croatia. *Geologica Carpathica* 58, 511–530.

Slovenec D., Lugović B. & Vlahović I. 2010: Geochemistry, petrology and tectonomagmatic significance of basaltic rocks from the ophiolite mélange at the NW external–internal Dinarides junction (Croatia). *Geologica Carpathica* 61, 273–294. https://doi.org/10.4154/GC.2015.03

Slovenec D., Lugović B., Meyer H.P. & Garapić-Šiftar G. 2011: A tectonomagmatic correlation of basaltic rocks from ophiolite mélanges at the north-eastern tip of the Sava-Vardar suture zone, northern Croatia, constrained by geochemistry and petrology. *Ofioliti* 36, 77–100.

Slovenec D., Šegvić B., Halamić J., Goričan Š. & Zanoni G. 2020: An ensialic volcanic arc along the northwestern edge of Palaeotethys – Insights from the Mid-Triassic volcano-sedimentary succession of Ivanščica Mt. (northwestern Croatia). *Geological Journal* 55, 4324–4351. https://doi.org/10.1002/gj.3664

Smirčić D., Kolar-Jurkovšek T., Aljinović D., Barudžija U., Jurkovšek B. & Hrvatović H. 2018: Stratigraphic definition and correlation of Middle Triassic volcaniclastic facies in the External Dinarides: Croatia and Bosnia and Herzegovina. *Journal of Earth Science* 29, 864–878. https://doi.org/10.1007/s12583-018-0789-1

Smirčić D., Aljinović D., Barudžija U. & Kolar-Jurkovšek T. 2020: middle Triassic syntectonic sedimentation and volcanic influence in the central part of the External Dinarides, Croatia (Velebit Mts.). *Geological Quarterly* 64, 220–239. https://doi.org/10.7306/gq.1528

Stampfli G.M. & Kozur H. 2006: Europe from the Variscan to the Alpine cycles. In: Gee D.G. & Stephenson R.(Eds.): European Lithosphere Dynamics. *Geological Society of London Memoir* 32, 57–82. https://doi.org/10.1144/GSL.MEM.2006.032.01.04

Storck J.-C., Brack P., Wotzlaw J.-F. & Ulmer P. 2019: Timing and evolution of Middle Triassic magmatism in the Southern Alps (northern Italy). *Journal of the Geological Society of London* 176, 253–268. https://doi.org/10.1144/jgs2018-123

Storck J.-C., Wotzlaw J.-F., Karakas Ö., Brack P., Gerdes A. & Ulmer P. 2020: Hafnium isotopic record of mantle-crust interaction in an evolving continental magmatic system. *Earth and Planetary Science Letters* 535, 116100. https://doi.org/10.1016/j.epsl.2020.116100

Streckeisen A. 1974: Classification and nomenclature of plutonic rocks. *Geologische Rundschau* 63, 773–786. https://doi.org/10.1007/BF01820841

Sun S.S. & McDonough W.F. 1989: Chemical and isotopic systematics of oceanic basalts: implications for mantle composition and processes. In: Saunders A.D. & Norry M.J. (Eds.): Magmatism in ocean basins. *Geological Society London Special Publication* 42, 313–345. https://doi.org/10.1144/GSL.SP.1989.042.01.19

Šikić K. 1995: Geological guidebook of Mt. Medvednica. [Geološki vodič Medvednice]. *Institut za geološka istraživanja, INA-Industrija nafte, Naftaplin Zagreb*, Zagreb, 1–199 (in Croatian).

Šikić K., Basch O. & Šimunić A. 1978: Basic Geological Map of Yugoslavia in scale 1:100,000, sheet Zagreb L38-80 [Osnovna geološka karta SFRJ M 1:100.000, list Zagreb L38-80]. *Geološki Institut Zagreb, Federal Geological Institute Beograd* (in Croatian).

Šikić K., Basch O. & Šimunić A. 1979: Explanatory notes for sheet Zagreb, L 33-80. [Tumač za list Zagreb L38-80]. *Geološki Institut Zagreb, Federal Geological Institute Beograd* (in Croatian).

Tomljenović B. 2002: Structural Characteristics of Medvednica and Samoborsko Gorje Mountains. [Strukturne značajke Medvednice i Samoborskog gorja]. *PhD Thesis, Univ. Zagreb*, 1–208 (in Croatian with English summary).

van Gelder I.E., Matenco L., Willingshofer E., Tomljenović B., Andriessen P.A.M., Ducea M.N. & Gruić A. 2015: The tectonic evolution of a critical segment of the Dinarides–Alps connection: Kinematic and geochronological inferences from the Medvednica Mountains, NE Croatia. *Tectonics* 34, 1952–1978. https://doi.org/10.1002/2015TC003937

von Richthofen F.F. 1860: Geognostische Beschreibung der Umgegend von Predazzo, Sanct Cassian und der Seisser Alpe in Süd-Tyrol. *Verlag von Justus Perthes*, Gotha, 1–327.

Wang X., Griffin W.L. & Chen J. 2010: Hf contents and Zr/Hf ratios in granitic zircons. *Geochemical Journal* 44, 65–72. https://doi.org/10.2343/geochemj.1.0043

Watson E.B. & Harrison T.M. 1983: Zircon saturation revisited: temperature and composition effects in a variety of crustal magma types. *Earth and Planetary Science Letters* 64, 295–304.

Watson E.B., Wark D.A. & Thomas J.B. 2006: Crystallization thermometers for zircon and rutile. *Contributions to Mineralogy and Petrology* 151, 413–433. https://doi.org/10.1007/s00410-006-0068-5

Wedepohl K.H. 1978: Handbook of Geochemistry. *Springer*, Berlin 1–442.

Wernicke B.P. 1992: Cenozoic extensional tectonics of the U. S. Cordillera. In: Burchfiel B.C., Lipman P.W. & Zoback M.L. (Eds.): Exposed cross-sections of the continental crust. *Kluwer*, Dordrecht, 509–544.

White R.W., Powell R., Holland T.J.B. & Worley B.A. 2000: The effect of TiO_2 and Fe_2O_3 on metapelitic assemblages at greenschist and amphibolite facies conditions: mineral equilibria calculations in the system K_2O–FeO–MgO–Al_2O_3–SiO_2–H_2O–TiO_2–Fe_2O_3. *Journal of Metamorphic Geology* 18, 497–511. https://doi.org/10.1046/j.1525-1314.2000.00269.x

White R.W., Powell R., Holland T.J.B., Johnson T.E. & Green E.C.R. 2014: New mineral activity–composition relations for thermodynamic calculations in metapelitic systems. *Journal of Metamorphic Geology* 31, 261–286. https://doi.org/10.1111/jmg.12071

Whitney D.L. & Evans B.W. 2010: Abbreviations for names of rock-forming minerals. *American Mineralogist* 95, 185–187. https://doi.org/10.2138/am.2010.3371

Zen E. & Hammarstrom J.M. 1984: Magmatic epidote and its petrologic significance. *Geology* 12, 515–518. https://doi.org/10.1130/0091-7613(1984)12<515:MEAIPS>2.0.CO;2

Supplement

Fig. S1. Outlined P–T occurrences and modal contents (isomodes in vol.%) of calculated mineral phases: **a** — garnet, **b** — amphibole, **c** — biotite, **d** — chlorite. Diagram is constructed with 3 wt.% H_2O in the bulk-rock composition.